Purinergic GPCR-integrin interactions drive pancreatic cancer cell invasion

Elena Tomas Bort [1,2], Megan D. Joseph[3,4], Qiaoying Wang[1], Edward P. Carter[1], Nicolas J. Roth[1,2], Jessica Gibson[1], Ariana Samadi[1], Hemant M. Kocher[1], Sabrina Simoncelli[3,4], [†]Peter J. McCormick[2], *[†]Richard P. Grose[1]

1. Centre for Tumour Biology, Barts Cancer Institute, Queen Mary University of London, London EC1M 6BQ, UK. 2. Centre for Endocrinology, William Harvey Research Institute, Queen Mary University of London. London EC1M 6BQ, UK 3. London Centre for Nanotechnology, University College London, London WC1H 0AH, UK 4. Department of Chemistry, University College London, London WC1H 0AJ, UK

*Corresponding author, [†]Co-senior Authors

Abstract

Pancreatic ductal adenocarcinoma (PDAC) continues to show no improvement in survival rates. One aspect of PDAC is elevated ATP levels, pointing to the purinergic axis as a potential attractive therapeutic target. Mediated in part by highly druggable extracellular proteins, this axis plays essential roles in fibrosis, inflammation response and immune function. Analysing the main members of the PDAC extracellular purinome using publicly available databases discerned which members may impact patient survival. *P2RY2* presents as the purinergic gene with the strongest association with hypoxia, the highest cancer cell-specific expression and the strongest impact on overall survival. Invasion assays using a 3D spheroid model revealed $P2Y_2$ to be critical in facilitating invasion driven by extracellular ATP. Using genetic modification and pharmacological strategies we demonstrate mechanistically that this ATP-driven invasion requires direct protein-protein interactions between $P2Y_2$ and αV integrins. DNA-PAINT super-resolution fluorescence microscopy reveals that $P2Y_2$ regulates the amount and distribution of integrin αV in the

plasma membrane. Moreover, receptor-integrin interactions were required for effective downstream signalling, leading to cancer cell invasion. This work elucidates a novel GPCR-integrin interaction in cancer invasion, highlighting its potential for therapeutic targeting.

Introduction

Pancreatic ductal adenocarcinoma (PDAC), which accounts for 90% of diagnosed pancreatic cancer cases, has the lowest survival rate of all common solid malignancies. Surgery is the only potentially curative treatment, yet more than 80% of patients present with unresectable tumours (Kocher, 2023). Consequently, most patients survive less than 6 months after diagnosis, resulting in a 5-year survival rate of less than 5% when accounting for all disease stages (Bengtsson, Andersson and Ansari, 2020; Kocher, 2023). Despite continued efforts, this statistic has improved minimally in the past 50 years. Due to increasing incidence, late detection and lack of effective therapies, pancreatic cancer is predicted to be the second most common cause of cancer-related deaths by 2040 (Rahib *et al.*, 2021).

Failure to significantly improve clinical management is mainly a result of chemoresistance (Neuzillet *et al.*, 2017), thus it is of vital importance to find new therapeutics that can improve patient survival. PDAC is characterised by its desmoplastic stroma, with dense fibrosis leading to impaired vascularisation and high levels of hypoxia (Koong *et al.*, 2000; Di Maggio *et al.*, 2016). Lack of oxygen leads to cellular stress and death, resulting in the release of purines such as ATP and adenosine into the tumour microenvironment (Forrester and Williams, 1977; Pellegatti *et al.*, 2008). Extracellular ATP concentration in PDAC is 200-fold more than normal tissue (Hu *et al.*, 2019), suggesting that purinergic signalling could represent an effective therapeutic target in pancreatic cancer.

The proteins underpinning purinergic signalling comprise several highly druggable membrane proteins involved in the regulation of extracellular purines, mainly ATP and adenosine (Burnstock and Novak, 2012; Boison and Yegutkin, 2019; Yu *et al.*, 2021). Extracellular ATP is known to promote inflammation (Kurashima *et al.*, 2012), growth (Ko *et al.*, 2012) and cell movement (Martinez-Ramirez *et al.*, 2016). Contrastingly, adenosine is anti-inflammatory and promotes immunosuppression (Schneider *et al.*, 2021). There are ongoing clinical trials in several cancers, including PDAC, for drugs targeting the ectonucleotidase CD73 (NCT03454451, NCT03454451) and adenosine receptor 2A (NCT03454451) in combination with PD-1 checkpoint inhibitors and/or chemotherapy. However, a Phase II multi-cancer study evaluating an anti-CD73 and anti-PD-L1 combination was withdrawn due to minimal overall clinical activity (NCT04262388). This suggests that the oncogenic impact of purinergic signalling may act via pathways other than immunosuppression and highlights the need for further mechanistic understanding of purinergic signalling in PDAC to exploit its full therapeutic potential.

Here we combine bioinformatic, genetic and drug-based approaches to identify a novel mechanism mediating ATP-driven invasion, uncovering a new therapeutic target in PDAC, a cancer of unmet clinical need. Beginning with an in-depth *in silico* analysis of the purinergic signalling transcriptome in PDAC, using publicly available patient and cell line databases, we build on bioinformatic data associating the purinergic receptor $P2Y_2$ with PDAC. After validating expression of $P2Y_2$ in human PDAC, we focus on identifying the function of the receptor in cancer cells. *In vitro* data underline the importance of $P2Y_2$ as a strong invasive driver, using a 3D physio-mimetic model of invasion. Finally, using a super-resolution imaging technique, DNA-PAINT, we characterise the behaviour of $P2Y_2$ in the membrane at the single molecule level, demonstrating the nanoscale distribution and

interaction of this receptor with RGD-binding integrins in promoting pancreatic cancer invasion.

Results

The PDAC extracellular purinome associates with patient survival, hypoxia score and cell phenotype.

The extracellular purinome encompasses 23 main surface proteins, including pannexin 1, P2X ion channels, ectonucleotidases, and the P2Y and adenosine GPCRs (Di Virgilio *et al.*, 2018) (Figure 1A). Interrogating public databases, we determined which purinergic signalling genes significantly impact pancreatic cancer survival. First, we examined the pancreatic adenocarcinoma (PAAD) database from The Cancer Genome Atlas (TCGA; n=177 patients), analysing overall survival hazard ratios based on purinergic signalling gene expression (Figure 1B). Expression of five purinergic genes correlated with decreased patient survival, with high *P2RY2* expression being associated with the highest hazard ratio (2.99, 95%, CI: 1.69 - 5.31, log-rank $p = 8.5 \times 10^{-5}$). We then examined the mutational profile and mRNA expression level of purinergic genes in patients. Using cBioPortal (Gao *et al.*, 2013), we generated OncoPrints of purinergic signalling genes from PAAD TCGA samples (Figure 1-figure supplement 1A), observing few genetic alterations in 0-3% of tumours and a heterogeneous percentage of tumours with high mRNA expression (z-score > 1) for each purinergic gene. PDAC molecular subtypes associated with purinergic signalling genes were varied (Supplementary file 1). In the Bailey model, most genes were related to the immunogenic subtype except for *NT5E*, *ADORA2B*, *PANX1* and *P2RY2*, which related to squamous (Bailey *et al.*, 2016). Collisson molecular subtyping showed several purinergic genes associated mostly to quasimesenchymal and exocrine subtypes (Collisson *et al.*, 2011). The Moffitt subtypes were not strongly associated with purinergic genes except for

ADA, *NT5E*, *P2RY6*, *P2RY2* and *PANX1* associated with the Basal subtype (Moffitt *et al.*, 2015).

PDAC is known for its hypoxic environment (Koong *et al.*, 2000; Yuen and Diaz, 2014), which is associated with worse overall survival (p = 0.002, Figure 1-figure supplement 1B); hypoxia can lead to cellular stress and death, resulting in increase of extracellular purines (Forrester and Williams, 1977). The Winter (Winter *et al.*, 2007), Ragnum (Ragnum *et al.*, 2015) and Buffa (Buffa *et al.*, 2010) hypoxia scores were used to examine the correlation between the expression of purinergic genes and hypoxia in the PAAD TCGA database (Figure 1-figure supplement 1C). Samples were divided into low (n=88) or high (n=89) hypoxia score, using the median hypoxia score to perform a differential expression analysis. CD73 (*NT5E*), adenosine A2B receptor (*ADORA2B*) and $P2Y_2$ (*P2RY2*) mRNA expression associated strongly with the high hypoxia score group for all three hypoxia scores ($\log_2$ ratio > 0.5, FDR < 0.0001). $P2Y_2$ had the highest $\log_2$ ratio in all hypoxia signatures compared to other purinergic genes. With a more extensive gene signature, the Winter hypoxia score (99 genes) allowed for a more comprehensive relative hypoxia ranking of tumour samples, compared to Ragnum (32 genes) and Buffa (52 genes) signatures. Hence, we used cBioPortal (Gao *et al.*, 2013) to generate a transcriptomic heatmap of purinergic genes, ranked using the Winter hypoxia score and overlaid with overall survival data (Figure 1C). Taken together, these results show a direct correlation between Winter hypoxia score and decreased overall survival for high hypoxia score-related purinergic genes.

We hypothesised that genes related to high hypoxia scores would be expressed preferentially in the tumour cell compartment, as PDAC cells inhibit angiogenesis, causing hypo-vascularisation in the juxta-tumoural stroma (Di Maggio *et al.*, 2016). Mining published

RNA-seq data from 60 paired PDAC samples of stroma and tumour microdissections (GSE93326) (Maurer *et al.*, 2019) and performing differential expression analysis, we observed that most genes related to high Winter hypoxia scores (*P2RY2*, *ADORA2B* and *NT5E*) were expressed in the tumour epithelial tissue (Figure 1D), except for *PANX1*, encoding for pannexin 1, which is involved in cellular ATP release (Bao, Locovei and Dahl, 2004).

To elucidate the cell type-specific purinergic expression landscape, we used published data from TCGA PAAD compartment deconvolution, using DECODER (Peng *et al.*, 2019) to plot purinergic gene weights for each cell type compartment (Figure 1E). The findings recapitulated the cell specificity data obtained from tumour microdissection analysis (Maurer *et al.*, 2019) (Figure 1D). Expression of purinergic genes in cancer cells was confirmed by plotting Z-scores of mRNA expression of PDAC cell lines from the cancer cell line encyclopaedia (Ghandi *et al.*, 2019) (CCLE; Figure 1-figure supplement 1D). Moreover, expression of purinergic genes in normal tissue from the Genotype-Tissue Expression (GTEx) database compared to cancer tissue (PAAD TCGA) also mimicked the results found with DECODER (Figure 1-figure supplement 1E). *P2RY2*, encoding $P2Y_2$ - a GPCR activated by ATP and UTP, was shown to be the purinergic gene most highly associated with cancer cell-specific expression in all our independent analyses (Figure 1D, E; Figure 1-figure supplement 1D, E). *P2RY2* additionally showed the strongest correlation with all hypoxia scores (Figure 1C; Figure 1-figure supplement 1C). Most importantly, of all purinergic genes, *P2RY2* expression had the biggest adverse impact on patient survival (Figure 1B). These independent *in silico* analyses encouraged us to explore the influence of $P2Y_2$ on pancreatic cancer cell behaviour.

P2RY2 is expressed in cancer cells and causes cytoskeletal changes.

144 To validate our bioinformatic findings, based on microdissections from a 60 patient cohort
145 (GSE93326) and from the deconvolution of 177 PAAD tissues from the TCGA, we
146 performed RNAscope on human PDAC samples. This corroborated $P2Y_2$ mRNA expression
147 as being localised to the epithelial tumour cell compartment and not stroma, normal
148 epithelium or endocrine tissues (n=3, representative images of 2 different patients shown in
149 Figure 2A and Figure 2-figure supplement 1A), matching our findings from larger publicly
150 available cohorts, including $P2Y_2$ IHC data from 264 patients in the Renji cohort (Hu *et al.*,
151 2019). $P2Y_2$ is known to be expressed at low levels in normal tissues but interestingly
152 RNAscope did not detect this. This data suggests 1) the lower limits of the technique
153 compounded by the challenge of RNA degradation in pancreatic tissue and 2) supports that
154 in tumour tissue where it was detected there was indeed overexpression of $P2Y_2$, in line
155 with the bioinformatic data. Interrogating single cell $P2Y_2$ RNA expression in normal PDAC
156 from proteinatlas.org (Karlsson *et al.*, 2021), expression was found at low levels in several
157 cells types, for example in endocrine cells and macrophages (Figure 2-figure supplement
158 1B). Using GEPIA (Tang *et al.*, 2017), we analysed PAAD TCGA and GTEx mRNA
159 expression of tumour (n=179) and normal samples (n=171). Tumour samples expressed
160 significantly higher ($p < 0.0001$) $P2Y_2$ mRNA levels compared to the normal pancreas
161 (Figure 2B). Kaplan-Meier analysis from PAAD TCGA KMplot (Lánczky and Győrffy, 2021)
162 showed a significant decrease in median overall survival in patients with high $P2Y_2$ mRNA
163 expression (median survival: 67.87 vs 17.27 months) (Figure 2C).

164 To predict $P2Y_2$ function in PDAC, we performed gene set enrichment analysis (GSEA) of
165 high vs low mRNA expressing $P2Y_2$ tumour samples, divided by the median expression, for
166 PAAD TCGA (n=177) and the PDAC Clinical Proteomic Tumour Analysis Consortium
167 (CPTAC) (n=140) databases. The top gene set enriched in the PANTHER pathway
168 database in both cohorts was ‘integrin signalling pathway’ (Figure 2D). The top four

enriched gene sets from the Gene Ontology 'Molecular function' functional database were associated with cell adhesion molecule binding, the cytoskeleton, protease binding and extracellular matrix binding (Figure 2-figure supplement 1C). As preliminary validation of the GSEA results *in vitro*, we used the PDAC cell line AsPC-1, transduced with Lifeact, a peptide which fluorescently labels filamentous actin structures (Riedl *et al.*, 2008), and monitored cell morphology using the Incucyte live-cell analysis system. Cells treated with ATP (100 μM) showed cytoskeletal rearrangements which were blocked by the selective $P2Y_2$ antagonist AR-C118925XX (AR-C; 5 μM; Figure 2E)(Muoboghare, Drummond and Kennedy, 2019). Exposing cells to ATP at 100 μM resulted in the biggest change in cell area when testing 6 concentrations from 0.01 to 1000 μM (Figure 2-figure supplement 1D). ATP-driven morphological changes were fully reversed at 5X (5 μM) the IC_{50} of AR-C (1 μM), while AR-C on its own had no effect on cell morphology (Figure 2-figure supplement 1E).

$P2Y_2$ is the only P2Y GPCR possessing an RGD motif, located in the first extracellular loop (Figure 2F). $P2Y_2$ has been shown to interact with αV integrins through this RGD motif (Erb *et al.*, 2001), but the significance of this interaction has not been explored in cancer. Immunofluorescence (IF) showed colocalisation of integrin αV and $P2Y_2$ in the PDAC cell lines AsPC-1 as well as PDAC cell lines with strong epithelial morphology, BxPC-3 and CAPAN-2, while MIA PaCa-2 cells showed low expression of both proteins, and PANC-1 showed high integrin αV and low $P2Y_2$, matching CCLE data (Figure 2G; Figure 2-figure supplement 1F, G). We hypothesized that $P2Y_2$, through its RGD motif, could engage αV integrins in cancer cells in the presence of ATP, leading to increased migration and invasion.

Targeting $P2Y_2$ and its RGD motif decreases ATP-driven invasion in PDAC cell lines.

193 To evaluate the impact of $P2Y_2$ in pancreatic cancer cell invasion, we used a 3D hanging
194 drop spheroid model (Murray *et al.*, 2022). PDAC cell lines were combined with stellate
195 cells in a ratio of 1:2 (Kadaba *et al.*, 2013), using an immortalised stellate cell line, PS-1
196 (Froeling *et al.*, 2009) to form spheres (Figure 3A), recapitulating the ratios of the two
197 biggest cellular components in PDAC. Stellate cells are crucial for successful hanging drop
198 sphere formation (Figure 3-figure supplement 1A) and cancer cell invasion (Murray *et al.*,
199 2022). Spheres were embedded in a Collagen type I and Matrigel mix and cultured for 48
200 hours until imaging and fixing (Figure 3A). Given that extracellular ATP concentration in
201 tumours is in the hundred micromolar range (Pellegatti *et al.*, 2008), spheres were treated
202 with $P2Y_2$ agonists ATP and UTP (100 μM). Both nucleotides increased invasion of the
203 PDAC cell line AsPC-1 significantly compared to vehicle control ($p < 0.0001$ and $p = 0.0013$
204 respectively), and this was blocked by the $P2Y_2$ selective antagonist AR-C (5 μM, $p =$
205 0.0237 and $p = 0.0133$; Figure 3B, C; Figure 3-figure supplement 1B). Treating spheres
206 with AR-C on its own did not show significant effects on invasion (Figure 3-figure
207 supplement 1B). Importantly, a non-hydrolysable ATP (ATPγS ;100 μM) showed similar
208 effects to ATP, implicating ATP and not its metabolites as the cause of the invasion (Figure
209 3-figure supplement 1C). Of note, IF staining of PS-1 cells showed negligible expression of
210 $P2Y_2$ (Figure 3-figure supplement 1D). To determine whether integrin association was
211 necessary for ATP-driven invasion, we treated spheres with 10 μM cyclic RGDfV peptide
212 (cRGDfV), which binds predominantly to αVβ3 to block integrin binding to RGD motifs
213 (Kapp *et al.*, 2017), such as that in $P2Y_2$ (Ibuka *et al.*, 2015). cRGDfV treatment reduced
214 ATP-driven motility significantly, both in 3D spheroid invasion assays ($p < 0.0001$) (Figure
215 3B, C) and in 2D Incucyte migration assays (Figure 3-figure supplement 1E, F) as did
216 treatment with AR-C. To ensure that this behaviour was not restricted to AsPC-1 cells,

217 experiments were corroborated in the epithelial-like BxPC-3 cell line (Figure 3-figure
218 supplement 1G, H) (Tan *et al.*, 1986).

219 To further verify that ATP-driven invasion was dependent on $P2Y_2$, we silenced $P2Y_2$
220 expression in AsPC-1 cells using siRNA (Figure 3D; Figure 3-figure supplement 1I),
221 abrogating the invasive response to ATP ($p < 0.0001$). $P2Y_2$ involvement in this
222 phenomenon was confirmed by generating a $P2Y_2$ CRISPR-Cas9 AsPC-1 cell line
223 ($P2Y_2^{CRISPR}$), which displayed a significant decrease in invasion compared to a control
224 guide RNA CRISPR cell line (CTR^{CRISPR}) in both ATP-treated ($p <0.0001$) and non-treated
225 ($p = 0.0005$) conditions (Figure 3F, E). Additionally, we tested the off-target effects of AR-C
226 in AsPC-1 $P2Y_2^{CRISPR}$ spheres and confirmed no significant difference in invasion compared
227 to control (Figure 3-figure supplement 1J). Together, these findings demonstrate that $P2Y_2$
228 is essential for ATP-driven cancer cell invasion.

229 To determine the importance of the RGD motif of $P2Y_2$ in ATP-driven invasion, we obtained
230 a mutant $P2Y_2$ construct, where the RGD motif was replaced by RGE ($P2Y_2^{RGE}$), which has
231 less affinity for αV integrins (Erb *et al.*, 2001). This mutant was transfected into AsPC-1
232 $P2Y_2^{CRISPR}$ cells and compared to cells transfected with wild-type $P2Y_2$ ($P2Y_2^{RGD}$; Figure 3-
233 figure supplement 1K). Only spheres containing $P2Y_2^{RGD}$ transfected cells demonstrated a
234 rescue of the ATP-driven invasive phenotype ($p < 0.0001$; Figure 3G, H), with $P2Y_2^{RGE}$
235 spheres not responding to ATP treatment. To ensure this behaviour was not influenced by
236 off target CRISPR effects, we repeated the experiment in PANC-1 cell line, which express
237 very low levels of $P2Y_2$, but high levels of integrin αV (Figure 2-figure supplement 1F, G).
238 No ATP-driven invasion was observed in PANC-1 cells transfected with an empty vector
239 (EV) or with $P2Y_2^{RGE}$ (Figure 3I, J). Only when transfecting PANC-1 cells with $P2Y_2^{RGD}$ was

ATP-driven invasion observed ($p < 0.0001$). These results demonstrate that the RGD motif of $P2Y_2$ is required for ATP-driven cancer cell invasion.

DNA-PAINT reveals RGD-dependent changes in $P2Y_2$ and integrin αV surface expression

To interrogate how $P2Y_2$ interacts with αV integrins, we examined the nanoscale organisation of $P2Y_2$ and αV proteins under different treatment conditions using a multi-colour quantitative super-resolution fluorescence imaging method, DNA-PAINT. DNA-PAINT is a single-molecule localisation microscopy (SMLM) method based on the transient binding between two short single-stranded DNAs - the 'imager' and 'docking' strands. The imager strand is fluorescently labelled and freely diffusing in solution, whilst the docking strand is chemically coupled to antibodies targeting the protein of interest. For DNA-PAINT imaging of $P2Y_2$ and integrin αV, proteins were labelled with primary antibodies chemically coupled to orthogonal docking sequences featuring a repetitive (ACC)n or (TCC)n motif, respectively (Figure 4A). The benefit of such sequences is to increase the frequency of binding events, which in turn allows the use of relatively low imager strand concentrations without compromising overall imaging times, whilst achieving high signal-to-noise ratio and single-molecule localisation precision (Strauss and Jungmann, 2020).

The repetitive binding of imager and docking DNA strands in DNA-PAINT causes the same protein to be detected multiple times with nearly identical coordinates, originating a cluster of single molecule localisation around the true position of the protein. In contrast to other SMLM approaches, it is possible to take advantage of the DNA-binding kinetics to stoichiometrically calculate the number of proteins detected in each cluster of single molecule localisations, via an approach known as qPAINT (Schnitzbauer *et al.*, 2017). As exemplified in Figure 4B (and detailed in the methods section), qPAINT relies on the first

order binding kinetics between individual imager and docking strands to determine the number copies of a protein that reside within a cluster of single-molecule localisations. The qPAINT index histograms obtained from $P2Y_2$ and αV DNA-PAINT data sets were fitted with a multi-peak Gaussian function, identifying peaks located at multiples of a qPAINT index value of $q_{i,1}$ 0.011 Hz and 0.009 for the $P2Y_2$ and αV docking-imager pairs, respectively (Figure 4C). These values were thus used to quantify the exact number of $P2Y_2$ and αV proteins in all the clusters of single-molecule localisation in the DNA-PAINT data sets. By combining qPAINT with spatial statistics, we recovered a good estimation of the ground truth position of all the proteins in the DNA-PAINT data and quantified protein clustering.

We have previously analysed GPCR oligomerisation quantitatively using DNA-PAINT super-resolution microscopy of $P2Y_2$ in AsPC-1 cells (Joseph *et al.*, 2021), where we observed a decrease in $P2Y_2$ oligomerisation upon AR-C treatment. Hence, we questioned whether the RGD motif in $P2Y_2$ affected receptor distribution and clustering. We imaged AsPC-1 $P2Y_2^{CRISPR}$ cells transfected with $P2Y_2^{RGD}$ or $P2Y_2^{RGE}$ in the absence or presence of 100 μM ATP for 1 hour (Figure 4D), observing a 42% decrease in the median density of $P2Y_2$ proteins at the membrane when $P2Y_2^{RGD}$ cells were treated with ATP, compared to control (p < 0.0001; Figure 4E). In contrast, although a slight decrease in the density of $P2Y_2$ proteins on $P2Y_2^{RGE}$ cells was observed following ATP treatment, this was not statistically significant (p = 0.1570). The density of $P2Y_2$ proteins and protein clusters in both $P2Y_2^{RGD}$ and $P2Y_2^{RGE}$ controls were equivalent (Figure 4E, F; p > 0.9999), indicating similar expression of the receptor at the surface in both control conditions. Interestingly, the density of $P2Y_2$ clusters decreased significantly in both conditions when treating with ATP (Figure 4F; 43% decrease, p < 0.0001 for $P2Y_2^{RGD}$ and 48% decrease, p = 0.0002 for

288 $P2Y_2^{RGE}$). We repeated these studies with normal AsPC-1 cells (untransfected and with
289 unaltered $P2Y_2$ expression) treated with ATP +/- cRGDfV, only observing a reduction of
290 $P2Y_2$ at the membrane with ATP alone (68% decrease, p <0.0001), while co-treatment with
291 cRGDfV prevented this change (p > 0.9999; Figure 4-figure supplement 1A, B). These
292 findings highlight that the RGD motif is required for αV integrin to control $P2Y_2$ levels at the
293 membrane.

294 Turning to αV integrins, we observed an increase in the density of αV molecules and αV
295 clusters at the membrane when stimulating $P2Y_2^{RGD}$ with ATP (165 αV molecules/ROI, IQR
296 = 162.75; 6.5 αV clusters/ROI, IQR = 8.75) compared to $P2Y_2^{RGD}$ without stimulation (58 αV
297 molecules/ROI, IQR = 41; 2.5 αV clusters/ROI, IQR = 2; p = 0.0003; Figure 4G, H). This
298 phenomenon was also observed with normal AsPC-1 cells, with significantly more αV
299 molecules and clusters (p = 0.0382 and p = 0.0349) detected following ATP stimulation
300 (Figure 4-figure supplement 1C, D). In absence of stimulation, $P2Y_2^{RGE}$ transfected cells
301 exhibited more αV molecules and clusters at the membrane (182 αV molecules/ROI, IQR =
302 262.75; 9 αV clusters/ROI IQR = 14) compared to $P2Y_2^{RGD}$ cells (p = 0.0003, p=0.0024,
303 respectively). However, treating $P2Y_2^{RGE}$ cells with ATP did not result in significant changes
304 in αV molecules and clusters (p = 0.7086; p = 0.1846). When the number of clusters was
305 normalised with the number of αV molecules, to obtain the percentage of αV in clusters
306 (Figure 4-figure supplement 1E), there was no significant difference between conditions (p
307 > 0.9999), indicating that the increase in the number of αV clusters was due to an increase
308 in the number of αV proteins at the membrane. Of note, the percentage of $P2Y_2$ clusters
309 significantly decreased in $P2Y_2^{RGE}$ cells when treated with ATP compared to all other
310 conditions (Figure 4-figure supplement 1F). Taken together, these data indicate an RGD
311 motif-dependent function of activated $P2Y_2$ in localising integrin αV to the membrane.

312 Nearest neighbour distance (NND) was used to analyse homo and heterotypic protein-
313 protein interactions between $P2Y_2$ and αV. NND ranges were selected by using the
314 approximate dimension of the antibodies (~14 nm)(Tan *et al.*, 2008), integrins (5-10
315 nm)(Lepzelter, Bates and Zaman, 2012) and GPCRs (~3 nm) (Figure 4-figure supplement
316 2A) and corroborating them with the NND histograms (Figure 4-figure supplement 2B) to
317 predict the NND range in nm indicating a protein-protein interaction. We detected a higher
318 percentage of integrin αV proteins in <50 nm proximity to $P2Y_2$ in $P2Y_2^{RGD}$ cells following
319 ATP stimulation (Figure 4I; 103 % increase, p = 0.0143). In contrast, $P2Y_2^{RGE}$ cells
320 stimulated with ATP showed a 43% decrease (p = 0.0101) in αV molecules in close
321 proximity to $P2Y_2$ in comparison to unstimulated cells. Analysing the percentage of αV
322 proteins with NND in the 20-100 nm range, we saw a similar pattern (Figure 4J). ATP-
323 stimulated $P2Y_2^{RGD}$ and unstimulated $P2Y_2^{RGE}$ cells showed an increased percentage of αV
324 proteins spaced at this range compared to untreated $P2Y_2^{RGD}$ cells (98% increase with p =
325 0.0132 and 89% increase with p = 0.0181). No significant changes were observed in NND
326 of <20 nm between αV proteins in any of the conditions (Figure 4K). In contrast, $P2Y_2^{RGD}$
327 molecules were in significantly closer proximity to each other compared to $P2Y_2^{RGE}$ in
328 control and stimulated conditions (p < 0.0001 and p = 0.007)(Figure 4L). In summary, our
329 SMLM studies demonstrate a reciprocal interaction between αV integrin and $P2Y_2$
330 receptors, where $P2Y_2$ can alter integrin localisation to the plasma membrane while αV
331 integrins influence activated $P2Y_2$ membrane localisation.

332 ***The RGD motif in $P2Y_2$ is involved in integrin signalling***

333 There is growing evidence of the importance of endosomal GPCR signalling and its
334 potential relevance in disease and therapeutic opportunities (Calebiro and Godbole, 2018).
335 As we identified the RGD motif in $P2Y_2$ having a possible role in receptor internalisation,

integrin dynamics and invasion, we proceeded to look at integrin signalling through phosphorylation of FAK (p-FAK) and ERK (p-ERK) from 0 to 1 hour after treating with 100 μM ATP. AsPC-1 cells displayed a significant increase of FAK and ERK phosphorylation after 15 minutes of ATP stimulation, which was abrogated by concomitant targeting of $P2Y_2$ with AR-C (Figure 5A). When impairing the RGD motif function in $P2Y_2$ with cRGDfV or by transfecting AsPC-1 $P2Y_2^{CRISPR}$ cells with the $P2Y_2^{RGE}$ mutant, p-FAK and p-ERK levels decreased (Figure 5 B, C). Collectively, targeting the RGD motif in $P2Y_2$ impairs receptor signalling and inhibits pancreatic cancer cell invasion.

Discussion

Improved molecular understanding of PDAC is vital to identify effective therapeutic approaches to improve patient survival. Purinergic signalling includes many druggable targets that have been related to hypoxia (Synnestvedt *et al.*, 2002), immunosuppression (Fong *et al.*, 2020), and invasion (Li *et al.*, 2015), but have been relatively underexplored in PDAC. In this study, we used publicly available databases to identify purinergic signalling genes that could be promising targets for PDAC, determining $P2Y_2$ as a driver of pancreatic cancer cell invasion. Extracellular ATP stimulated invasion in a 3D spheroid model of PDAC; an effect blocked by targeting $P2Y_2$ genetically and pharmacologically. Mechanistically, we identified that the RGD motif in the first extracellular loop of $P2Y_2$ is required for ATP-driven cancer invasion. Importantly, quantitative DNA-PAINT super-resolution fluorescence microscopy revealed a role of this RGD motif in orchestrating the number of $P2Y_2$ and αV integrin proteins at the plasma membrane, upon ATP stimulation.

Purinergic signalling has been associated classically with hypoxia and immune function in cancer (Di Virgilio *et al.*, 2018). One of the first reports of hypoxia inducing ATP release in cells identified an increase of extracellular ATP in rat heart cells when kept in hypoxic

conditions (Forrester and Williams, 1977). PDAC is a highly hypoxic cancer, with high levels of ATP reported in the tumour interstitial fluid of human and mouse PDAC tissues compared to healthy tissues (Hu *et al.*, 2019). This vast release of ATP results in immune-mediated inflammatory responses via immune cells expressing purinergic signalling receptors (Chiarella *et al.*, 2021). Expression of most purinergic genes was associated predominantly with immune cells, immunogenic PDAC subtype and low hypoxia scores (Figure 1C, E). In contrast, expression of genes correlated with worse survival and hypoxia (*PANX1*, *NT5E*, *ADORA2B* and *P2RY2*) was associated with tumour cells and the squamous PDAC subtype, correlating with hypoxia, inflammation and worse prognosis (Bailey *et al.*, 2016). The role of CD73 in PDAC has been examined in several studies (Yu *et al.*, 2021) (NCT03454451, NCT03454451). In contrast, adenosine A_{2B} receptor has not been well studied. Adenosine A_{2B} receptor requires larger agonist concentrations for activation compared to other receptors in the same family, such as adenosine A_{2A} (Bruns, Lu and Pugsley, 1986; Xing *et al.*, 2016), and receptor expression has been reported to increase when cells are subjected to hypoxia (Feoktistov *et al.*, 2004). Moreover, HIF-1α has been shown to upregulate A_{2B} and $P2Y_2$ expression in liver cancer (Tak *et al.*, 2016; Kwon *et al.*, 2019). From our analyses, $P2Y_2$ was associated with the worst patient overall survival, highest patient hypoxia scores and strongest correlation with cancer cell expression compared to other purinergic genes. These observations were supported by published immunohistochemical staining of 264 human PDAC samples, showing that $P2Y_2$ localised predominantly in cancer cells in human PDAC and that $P2Y_2$ activation with ATP led to elevated HIF-1α expression (Hu *et al.*, 2019). Hence, we decided here to explore $P2Y_2$ in greater depth.

$P2Y_2$ has been associated with cancer cell growth and glycolysis in PDAC (Ko *et al.*, 2012; Hu *et al.*, 2019; Wang *et al.*, 2020). Combination treatment of subcutaneous xenografts of

385 AsPC-1 or BxPC-3 cells with the $P2Y_2$ antagonist AR-C together with gemcitabine
386 significantly decreased tumour weight and resulted in increased survival compared to
387 placebo or gemcitabine monotherapy control (Hu *et al.*, 2019). Surprisingly, GSEA results
388 of two different cohorts suggested a possible additional function of $P2Y_2$ in invasion.
389 Increased glycolysis and cytoskeletal rearrangements have been linked (Park *et al.*, 2020),
390 and both events could occur downstream of $P2Y_2$ activation. $P2Y_2$ has been implicated in
391 invasive phenotypes in prostate, breast and ovarian cancer (Jin *et al.*, 2014; Li *et al.*, 2015;
392 Martinez-Ramirez *et al.*, 2016). Moreover, high $P2Y_2$ expression in patients was related to
393 integrin signalling. The RGD motif in the first extracellular loop of $P2Y_2$ results in a direct
394 interaction of $P2Y_2$ with RGD-binding integrins, particularly integrins αVβ3 and αVβ5 (Erb et
395 al., 2001; Ibuka et al., 2015). This interaction can exert phenotypic effects – for example,
396 binding of $P2Y_2$ to integrins via its RGD motif is necessary for tubule formation in epithelial
397 intestinal cell line 3D models (Ibuka *et al.*, 2015). We focus here on the importance of the
398 RGD motif of $P2Y_2$ and its key for integrin interaction in a cancer context. We were able to
399 abrogate ATP-driven invasion using either the $P2Y_2$ selective antagonist AR-C or by
400 blocking $P2Y_2$-integrin complexes using the selective αVβ3 cyclic RGD-mimetic peptide
401 inhibitor cRGDfV. Likewise, spheres made using ASPC-1 $P2Y_2^{CRISPR}$ or PANC-1 cells
402 transfected with mutant $P2Y_2^{RGE}$, which decreases the affinity of $P2Y_2$ for integrins, did not
403 invade in response to ATP stimulation. Altogether, these results 1) support $P2Y_2$
404 involvement in PDAC cell invasion, 2) show the RGD motif is essential for this function, and
405 3) identify the mechanism for this to be caused by $P2Y_2$-integrin complexes. Despite efforts,
406 there are currently no clinically efficacious $P2Y_2$ antagonists, with poor oral bioavailability
407 and low selectivity being major issues (Neumann *et al.*, 2022). Our findings demonstrate
408 that $P2Y_2$ can also be targeted by blocking its interaction with RGD-binding integrins, due to
409 its dependence on integrins for its pro-invasive function.

GPCR-integrin crosstalk is involved in many biological processes (Wang *et al.*, 2005; Teoh *et al.*, 2012). Only one study has directly examined the spatial distribution of integrins and GPCRs, however this relied on IF analysis (Erb *et al.*, 2001), where only changes in the micron scale will be perceived, hence losing information of the nanoscale distances and individual protein interactions. Here, we present a method to image integrin and GPCR dynamics using quantitative DNA-PAINT super-resolution fluorescence microscopy (Schnitzbauer *et al.*, 2017), allowing spatial and quantitative assessment of $P2Y_2$ and integrin αV interactions at the single protein level. Following ATP stimulation, the number of $P2Y_2$ proteins at the plasma membrane decreased significantly after one hour, implying receptor internalisation, in line with previous work showing $P2Y_2$ at the cell surface was reduced significantly after one hour of UTP stimulation (Tulapurkar *et al.*, 2005). Of note, cytoskeletal rearrangements, which we have also observed upon ATP stimulation (Figure 2E), were required for $P2Y_2$ clathrin-mediated internalisation and authors noted that $P2Y_2$ was most likely in a complex with integrins and extracellular matrix-binding proteins. Cells expressing RGE mutant $P2Y_2$ or treated with cRGDfV, did not show significant changes in $P2Y_2$ levels at the membrane upon ATP treatment, thus implicating the RGD motif in $P2Y_2$ in agonist-dependent receptor internalisation, though we have focused on motility phenotype in this work.

$P2Y_2$ affecting cell surface redistribution of αV integrin has been reported, with αV integrin clusters observed after 5 min stimulation with UTP (Chorna *et al.*, 2007). We observed an increased number of αV integrin molecules and clusters one hour after ATP stimulation, although this increase in clusters was mainly due to the increase in total number of αV integrins at the membrane. The distance between αV integrin and $P2Y_2$ molecules decreased (NND < 50 nm) with ATP stimulation, indicating possible interaction. In contrast, with mutant $P2Y_2^{RGE}$, no significant ATP-dependent changes in the number of $P2Y_2$ or αV

integrin proteins at the membrane were observed. The same phenomenon was observed when treating normal AsPC-1 cells (untransfected and with no alteration to $P2Y_2$) with cRGDfV and ATP. We speculate that by reducing the ability of integrins to bind to the RGD of $P2Y_2$, through receptor internalisation, RGE mutation or through cRGDfV treatment, there is less RGD-triggered integrin endocytosis, hence less integrin recycling and an increase of integrins at the cell surface. Western blot results supported our postulated role of the RGD motif in $P2Y_2$ regulating downstream integrin signalling through FAK and ERK, leading to cancer cell migration and invasion (Figure 5,6). This is the first single-molecule super-resolution study to explore integrin and GPCR dynamics, and to demonstrate a requirement for integrin-$P2Y_2$ interactions in cancer cell invasion.

In summary, our study demonstrates that $P2Y_2$, via its RGD motif, has a pivotal role in ATP-induced PDAC invasion through interacting with, and regulating the number of αV integrins at the plasma membrane, revealing this critical axis as a promising therapeutic target.

Methods

Data mining and bioinformatic analysis

Hazard ratios and the $P2Y_2$ Kaplan-Meier plot for overall survival were obtained using Kaplan-Meier Plotter (RRID:SCR_018753) (Lánczky and Győrffy, 2021) and the pancreatic adenocarcinoma dataset from the cancer genome atlas (PAAD TCGA, RRID:SCR_003193).

Using cBioPortal (RRID:SCR_014555) (Gao *et al.*, 2013) and the database PAAD TCGA, mRNA differential expression analysis was performed for each Hypoxia Score (Winter *et al.*, 2007; Buffa *et al.*, 2010; Ragnum *et al.*, 2015) by separating patients using the median hypoxia score. Results from purinergic genes were plotted in a volcano plot using

458 VolcaNoseR (Goedhart and Luijsterburg, 2020). Significant hits were plotted in a heat map
459 using cBioPortal (Gao *et al.*, 2013). RNAseq raw counts from stromal and epithelial PDAC
460 tissue from microdissections were downloaded from the GEO database (GSE93326)
461 (Maurer *et al.*, 2019) and a differential expression analysis was performed using DESeq2
462 (RRID:SCR_015687) (Love, Huber and Anders, 2014; Varet *et al.*, 2016) in R.

463 Gene weight results from DECODER from PDAC tissues in the TCGA database were
464 obtained from published results (Peng *et al.*, 2019). Using GEPIA (RRID:SCR_018294)
465 (Tang *et al.*, 2017), mRNA expression of purinergic genes in normal tissue from the
466 Genotype-Tissue Expression (GTEx, RRID:SCR_013042) compared to cancer tissue
467 (PAAD TCGA) was obtained. PDAC cell line mRNA z-scores or mRNA reads per kilobase
468 million (RPKM) were obtained using cBioPortal and the Cancer Cell Line Encyclopaedia
469 (CCLE, RRID:SCR_013836) data (Gao *et al.*, 2013).

470 For gene set enrichment analysis (GSEA), cBioPortal was used to separate PAAD TCGA or
471 PDAC CPTAC patients into high and low *P2RY2* by *P2RY2* median expression and perform
472 the differential expression analysis. Log ratio values were inserted in the WEB-based Gene
473 SeT AnaLysis Toolkit (WebGestalt, RRID:SCR_006786) (Liao *et al.*, 2019), where 'GO:
474 Molecular Function' or 'Panther' with default analysis parameters were selected.

475 **RNAscope® *in-situ* hybridisation**

476 Formalin-fixed paraffin embedded (FFPE) sections (n=3) of PDAC with stroma and normal
477 adjacent tissue were obtained from the Barts Pancreas Tissue Bank (Project
478 2021/02/QM/RG/E/FFPE). Sections were stained using the human *P2RY2* probe (853761,
479 ACD) and the RNAscope® 2.5 HD Assay-RED (ACD) following manufacturer's instructions.
480 Slides were imaged by NanoZoomer S210 slide scanner (Hamamatsu).

Cell lines and cell culture

The pancreatic cancer cell lines AsPC-1 (RRID:CVCL_0152) , BxPC-3 (RRID:CVCL_0186) , MIA PaCa-2 (RRID:CVCL_0428) and PANC-1 (RRID:CVCL_0480), in addition to the immortalised stellate cell line PS-1 (Froeling *et al.*, 2009) were kindly donated by Prof. Hemant Kocher (Queen Mary University of London). Cell lines stably expressing fluorescently labelled histone subunits (H2B) or Lifeact (Riedl *et al.*, 2008) were transduced with viral supernatant obtained from HEK293T cells co-transfected with pCMVR8.2 (Addgene #12263) and pMD2.G (Addgene #12259) packaging plasmids, and either H2B-GFP (Addgene #11680), H2B-RFP (Addgene #26001) or Lifeact-EGFP (Addgene # 84383) plasmids using FuGENE transfection reagent (Promega), following manufacturer's guidelines. Successfully transduced cells were isolated using a BD FACS Aria Fusion cell sorter. AsPC-1 $P2Y_2^{CRISPR}$ cells were generated by transfecting cells with a dual gRNA (TGAAGGGCCAGTGGTCGCCGCGG and CATCAGCGTGCACCGGTGTCTGG) CRISPR-CAS9 plasmid (VectorBuilder) with an mCherry marker which was used to select successfully transfected cells as above. Clonal expansion of single sorted cells was achieved with serial dilution cloning. Clones were evaluated by IF for $P2Y_2$ compared to parental AsPC-1 cells. Cell lines were grown at 37 ºC with 5% CO_2 in DMEM (Gibco), RPMI-1640 (Gibco) or DMEM/F-12 (Sigma) supplemented with 10% fetal bovine serum (Sigma). Cells were monitored for mycoplasma contamination every six months.

Cell fixation and immunofluorescent staining

Cells were seeded on coverslips placed in a 6 well-plate (Corning) and fixed the next day in 4% paraformaldehyde (LifeTech) for 30 min and washed 3x with phosphate buffered saline (PBS). Coverslips were placed in 0.1% Triton X-100 (Avantor) for 10 min for permeabilization, followed by 3 PBS washes and blocking with 5% bovine serum albumin

(BSA; Merck) for 1 hour. Coverslips were incubated at 4 ºC overnight with anti-$P2Y_2$ (APR-010, Alomone labs) and anti-integrin αV antibodies (P2W7, Santa Cruz) diluted in blocking solution (1:100 and 1:200, respectively). After 3 PBS washes, coverslips were incubated for 1 hour with Alexa Fluor 647 goat anti-mouse and Alexa Fluor 488 goat anti-rabbit (Invitrogen) or Alexa Fluor 546 goat anti-rabbit at 1:1000, diluted in blocking buffer. Following 3 PBS washes, 4',6-diamidino-2-phenylindole (DAPI, Sigma-Aldrich) was used as a nuclear stain and was incubated for 10 min. Slides were mounted using Mowiol (Calbiochem) and imaged 24 hours later using a LSM 710 confocal microscope (Zeiss).

siRNA and plasmid transfection

Cells were seeded in 6 well plates at a density of 200,000 cells/well 24 hours before transfection. For siRNA experiments, cells were transfected with 20 nM pooled control or $P2Y_2$-targeting siRNAs from a siGENOME SMARTpool (Dharmacon, GE Heathcare) with Lipofectamine 3000 (Invitrogen) following manufacturer's instructions. For $P2Y_2$ plasmid expression experiments, cells were transfected with 500 nM *P2RY2* ($P2Y_2^{RGD}$) or *P2RY2D97E* ($P2Y_2^{RGE}$) in pcDNA3.1 vector (Obtained from GenScript) or pcDNA3.1 alone (Empty vector, EV) together with lipofectamine 3000 and p3000 reagent (Invitrogen) as per manufacturer's instructions. Plasmid concentration was selected by comparing AsPC-1 IF staining of $P2Y_2$ with IF staining in AsPC-1 $P2Y_2^{CRISPR}$ and PANC-1 cells with different concentrations of plasmid to achieve a similar IF signal. Cells were split 48 hours post-transfection for experiments or imaged 72 hours post-transfection.

3D sphere model invasion assay

Spheres of PDAC cell lines with PS-1 cells were generated as described (Murray *et al.*, 2022). Cancer cells at 22,000 cells/mL and PS-1 cells at 44,000 cells/mL were combined

with DMEM/F-12 and 1.2% methylcellulose in a 4:1 ratio of methylcellulose (Sigma-Aldrich) and 20 µl drops, each containing 1000 cells, pipetted on the underside of a 15 cm dish lid (Corning) and hanging drops were incubated overnight at 37 ºC. The next day, spheres were collected and centrifuged at 300 g for 4 minutes and washed with medium. A mix of 2 mg/mL collagen (Corning), 175 µL/mL Matrigel, 25 µL/mL HEPES (1M, pH 7.5) and 1N NaOH (for neutral pH correction) was prepared with DMEM/F12 medium. Spheroids were re-suspended and seeded in low attachment 96-well plates (50 µl per well) with 40 µL previously gelled mix in the bottom of the wells. Once set, 150 µL of DMEM/F12 was added with treatments. Spheres were treated with 100 µM adenosine 5'-triphosphate trisodium salt hydrate (ATP, Sigma), uridine 5'-triphosphate trisodium salt hydrate (UTP, Sigma) or adenosine 5'-[γ-thio]triphosphate tetralithium salt (ATPγS, Tocris) alone or with 5 µM AR-C118925XX (AR-C, Tocris) or 10 µM cyclo(RGDfV) (cRGDfV, Sigma-Aldrich). Treatments were repeated 24 hours later. Spheres were imaged with a Zeiss Axiovert 135 light microscope at 10x on day 2 after seeding. Cells were stained with 4',6-diamidino-2-fenilindol (DAPI) (1:1000) for 10 minutes and imaged with a Zeiss LSM 710 confocal microscope. %Invasion was calculated by drawing an outline around the total area A_{total} and central area $A_{central}$ of the spheres with ImageJ (Fiji) and using the equation:

$$\%Invasion = \left(\frac{A_{total} - A_{central}}{A_{central}}\right) x100$$

Results were plotted in SuperPlots by assigning different colours to repeats and superimposing a graph of average % Invasion with a darker shade of the assigned colour as described previously (Lord *et al.*, 2020).

IncuCyte migration assay

In IncuCyte ClearView 96-well cell migration plates (Essen BioScience), 40 µL medium with 5,000 cells were seeded in each well. A solution of 20 µL medium with 15 µM AR-C or 30 µM cRGDfV was added on top of the wells to achieve a final concentration of 5 µM and 10 µM respectively. Cells were allowed to settle for 15 minutes at room temperature and then placed at 37 ºC for pre-incubation with the treatments for another 15 min. A volume of 200 µL of medium with or without 100 µM ATP was added in the appropriate reservoir wells and the plate was placed in the IncuCyte S3 (Essen BioScience) and was monitored every 4 hours for 39 hours (average doubling time of AsPC-1 cells (Chen *et al.*, 1982)). Using the IncuCyte S3 2019A software, the migration index was calculated by analysing the average area occupied by the cells in the bottom well and was averaged with the initial average area occupied by cells in the top well.

RNA extraction and qPCR analysis

RNA was extracted using the Monarch RNA extraction kit (New England BioLabs) as instructed by the manufacturer. The extracted RNA was quantified using a Nanodrop One Spectrophotometer (ThermoFisher Scientific). Using LunaScript RT Supermix kit (BioLabs), cDNA was prepared in a 20 µL reaction according to manufacturer's instructions. The resulting cDNA was used in conjunction with MegaMix-Blue and *P2RY2* primers (Eurogentec; Forward sequence: GCTACAGGTGCCGCTTCAAC, reverse sequence: AGACACAGCCAGGTGGAACAT)(Hu *et al.*, 2019) for quantitative polymerase chain reaction (qPCR) at the manufacturer's recommended settings in a StepOnePlus Real-Time PCR System (Applied Biosystems). The relative mRNA expression was calculated using the $2^{-\Delta\Delta Ct}$ method (Livak and Schmittgen, 2001) and normalised to GAPDH.

DNA-antibody coupling reaction

572 DNA labelling of anti-αV antibody (P2W7, Santa Cruz, RRID:AB_627116) and anti-
573 $P2Y_2$ receptor antibody (APR-010, Alomone labs, RRID:AB_2040078) was performed via
574 maleimidePEG2-succinimidyl ester coupling reaction as previously described (Simoncelli *et*
575 *al.*, 2020; Joseph *et al.*, 2021) . Firstly, 30 µL of 250 mM DDT (Thermo Fisher Scientific)
576 was added to 13 µL of 1 mM thiolated DNA sequences 5′-Thiol-AAACCACCACCACCA-3′
577 (Docking 1), and 5-Thiol-TTTCCTCCTCCTCCT-3' (Docking 2) (Eurofins). The reduction
578 reaction occurred under shaking conditions for 2 hours. 30 min after the reduction of the
579 thiol-DNA started, 175 µL of 0.8 mg/mL antibody solutions were incubated with 0.9 µL of
580 23.5 mM maleimide-PEG2-succinimidyl ester cross-linker solution (Sigma-Aldrich) on a
581 shaker for 90 min at 4 °C in the dark. Prior DNA-antibody conjugation, both sets of
582 reactions were purified using Microspin Illustra G-25 columns (GE Healthcare) and Zeba
583 spin desalting columns (7K MWCO, Thermo Fisher Scientific), respectively, to remove
584 excess reactants. Next, coupling of anti-$P2Y_2$ with with DNA docking 1 and anti-αV with
585 DNA Docking 2 was performed by mixing the respective flow-through of the columns and
586 incubate them overnight, in the dark, at 4°C under shaking. Excess DNA was removed via
587 Amicon spin filtration (100K, Merck) and antibody-DNA concentration was measured using
588 a NanoDrop One spectrophotometer (Thermo Fisher Scientific) and adjusted to 10 µM with
589 PBS. Likewise, spectrophotometric analysis was performed to quantify the DNA-antibody
590 coupling ratio and found to be ~1.2 in average for both the oligo-coupled primary
591 antibodies.

592

593 **Cell fixation and immunofluorescence staining for DNA-PAINT imaging**

594 Cells were seeded at 30,000 cells per channel on a six-channel glass bottomed microscopy
595 chamber (µ-SlideVI$^{0.5}$, Ibidi) pre-coated with rat tail collagen type I (Corning). The chamber

was incubated at 37 ºC for 8 hours before treatments. Cells were treated with 100 µM of ATP (or the equivalent volume of PBS as control) in medium for 1 hour and were fixed and permeabilised as described in the 'Cell fixation and immunofluorescent staining' section. Following permeabilization, samples were treated with 50 mM ammonium chloride solution (Avantor) for 5–10 min to quench auto-fluorescence and cells were washed 3× in PBS. Blocking was completed via incubation with 5% BSA (Merck) solution for 1 hour followed by overnight incubation at 4°C with 1:100 dilutions of DNA labelled anti-$P2Y_{2,}$ and DNA labelled anti-αV antibody in blocking solution. The next day, samples were washed 3× in PBS and 150 nm gold nanoparticles (Sigma-Aldrich) were added for 15 min to act as fiducial markers for drift correction, excess of nanoparticles was removed by 3× washes with PBS. Samples were then left in DNA-PAINT imager buffer solution, prepared as described below, and immediately used for DNA-PAINT imaging experiments.

DNA-PAINT imager solutions

A 0.1 nM $P2Y_2$ imager strand buffer solution (5-TTGTGGT-3'-Atto643, Eurofins) and a 0.2 nM αV imager strand buffer solution (5-GGAGGA-3'-Atto643, Eurofins) were made using 1× PCA (Sigma-Aldrich), 1× PCD (Sigma-Aldrich), 1× Trolox (Sigma-Aldrich), 1× PBS and 500 mM NaCl (Merck) which facilitates establishment of an oxygen scavenging and triplet state quencher system. Solutions were incubated for 1 h in the dark before use. Stock solutions of PCA, PCD and Trolox were prepared as follows: 40× PCA (protocatechuic acid) stock was made from 154 mg of PCA (Sigma-Aldrich) in 10 mL of Ultrapure Distilled water (Invitrogen) adjusted to pH 9.0 with NaOH (Avantor, Radnor Township, PA, USA). 100x PCD (protocatechuate 3,4-dioxygenase) solution was made by adding 2.2 mg of PCD (Sigma-Aldrich) to 3.4 mL of 50% glycerol (Sigma-Aldrich) with 50 mM KCl (Sigma-Aldrich), 1 mM EDTA (Invitrogen), and 100 mM Tris buffer (Avantor). 100x

Trolox solution was made by dissolving 100 mg of Trolox in 0.43 mL methanol (Sigma-Aldrich), 0.345 mL 1 M NaOH, and 3.2 mL of Ultrapure Distilled water.

Exchange-PAINT Imaging Experiments

Exchange DNA-PAINT imaging was performed on a custom built total internal reflection fluorescence (TIRF) microscope based on a Nikon Eclipse Ti-2 microscope (Nikon Instruments) equipped with a 100× oil immersion TIRF objective (Apo TIRF, NA 1.49) and a Perfect Focus System. Samples were imaged under flat-top TIRF illumination with a 647 nm laser (Coherent OBIS LX, 120 mW), that was magnified with custom-built telescopes, before passing through a beam shaper device (piShaper 6_6_VIS, AdlOptica) to transform the Gaussian profile of the beam into a collimated flat-top profile. The beam was focused into the back focal plane of the microscope objective using a suitable lens (AC508-300-A-ML, Thorlabs), passed through a clean-up filter (FF01-390/482/563/640-25, Semrock) and coupled into the objective using a beam splitter (Di03-R405/488/561/635-t1-25×36, Semrock). Laser polarization was adjusted to circular after the objective. Fluorescence light was spectrally filtered with an emission filter (FF01-446/523/600/677-25, Semrock) and imaged on a sCMOS camera (ORCA-Flash4.0 V3 Digital, Hamamatsu) without further magnification, resulting in a final pixel size of 130 nm in the focal plane, after 2 × 2 binning. For fluid exchange each individual chamber of the ibidi μ-SlideVI$^{0.5}$ were fitted with elbow Luer connector male adaptors (Ibidi) and 0.5 mm silicon tubing (Ibidi). Each imaging acquisition step was performed by adding the corresponding imager strand buffer solution to the sample. Prior to imager exchange, the chamber was washed for 10 min with 1x PBS buffer with 500 mM NaCl. Before the next imager strand buffer solution was added, we monitored with the camera to ensure complete removal of the first imager strand. Sequential imaging and washing steps were repeated for every cell imaged. For each

644 imaging step, 15,000 frames were acquired with 100 ms integration time and a laser power
645 density at the sample of 0.5 kW/cm^2.

646 **Super resolution DNA-PAINT image reconstruction**

647 Both $P2Y_2$ and αV Images were processed and reconstructed using the Picasso
648 (Schnitzbauer *et al.*, 2017) software (Version 0.3.3). The Picasso 'Localize' module was
649 used to identify and localise the x,y molecular coordinates of single molecule events from
650 the raw fluorescent DNA-PAINT images. Drift correction and multi-colour data alignment
651 was performed via the Picasso 'Render' module, using a combination of fiducial markers
652 and multiple rounds of image sub-stack cross correlation analysis. Localisations with
653 uncertainties greater than 13 nm were removed and no merging was performed for
654 molecules re-appearing in subsequent frames. Super-resolution image rendering was
655 performed by plotting each localization as a Gaussian function with standard deviation
656 equal to its localization precision.

657 **Protein quantification via qPAINT analysis**

658 To convert the list of *x,y* localisations into a list of *x,y* protein coordinates the data was
659 further processed using a combination of DBSCAN cluster analysis, qPAINT analysis and
660 *k*-means clustering.

661 First, 21 randomly selected, non-overlapping, 4x4 μm^2 regions on interest (ROIs) for each
662 type of cell and cell treatment were analysed with a density-based clustering algorithm,
663 known as DBSCAN. To avoid suboptimal clustering results; ROIs were selected such that
664 they do not intersect with cell boundaries and the regions were the same for $P2Y_2$ and αV
665 images. Single molecule localisations within each ROIs were grouped into clusters using
666 the DBSCAN modality from PALMsiever (Pengo, Holden and Manley, 2015) in MATLAB

667 (Version 2021a)(Pengo, Holden and Manley, 2015). This clustering algorithm determines
668 clusters based upon two parameters. The first parameter is the minimum number of points
669 ('minPts') within a given circle. For minPts we chose a parameter in accordance to the
670 binding frequency of the imager strand and acquisition frame number; in our case this was
671 set to 10 localisations for all the experiments. The second parameter is the radius (epsilon
672 or 'eps') of the circle of the cluster of single molecule localisations. This is determined by
673 the localisation precision of the super-resolved images and, according to the nearest
674 neighbour based analysis was ca. to 10 nm for all the images.

675 For qPAINT analysis we used a custom-written MATLAB (Version 2021a) code:
676 https://github.com/Simoncelli-lab/qPAINT_pipeline (Joseph and Simoncelli, 2023). Briefly,
677 localisations corresponding to the same cluster were grouped and their time stamps were
678 used to compile the sequence of dark times per cluster. All the dark times per cluster were
679 pooled and used to obtain a normalised cumulative histogram of the dark times which was
680 then fitted with the exponential function $1 - \exp(t/\tau_d)$ to estimate the mean dark time, τ_d, per
681 cluster. The qPAINT index (q_i) of each cluster was then calculated as the inverse of the
682 mean dark time, $1/\tau_d$.

683 Calibration was then performed via compilation of all qPAINT indexes obtained from the
684 DNA-PAINT data acquired for each protein type into a single histogram. Only qPAINT
685 indices corresponding to small clusters (i.e., cluster with a maximum point distance of 150
686 nm) were considered. This histogram was fitted with a multi-peak Gaussian function to
687 determine the qPAINT index for a cluster of single molecule localisations corresponding to
688 one protein (q_{i1}).

689 The calibration value obtained with this method was used to estimate the number of $P2Y_2$
690 and αV proteins in all the single molecule localisations clusters identified by DBSCAN, as

this corresponds to the ratio between q_{i1} and the qPAINT index of each cluster. Finally, *k*-means clustering was used to recover a likely distribution of the proteins' positions in each cluster of single molecule localisations, where *k* is equal to the number of proteins in that cluster. This information allowed us to quantify the protein density and level of protein clustering.

Nearest neighbour analysis

Nearest neighbour distances (NND) for $P2Y_2$ – $P2Y_2$ and αV-αV were calculated using the recovered $P2Y_2$ and αV-protein maps as described above via a custom-written MATLAB (Version 2021a) script: https://github.com/Simoncelli-lab/qPAINT_pipeline (Joseph and Simoncelli, 2023). For colocalisation analysis, the NND for each protein of one dataset with respect to the reference dataset was calculated (i.e., $P2Y_2$ - αV) using a similar MATLAB script. To evaluate the significance of the NND distributions, we randomized the positions of $P2Y_2$ and αV for the comparison of $P2Y_2$ – $P2Y_2$ and αV-αV NND distributions, respectively, and the positions of one of the two proteins for the comparison of the NND between $P2Y_2$ - αV protein distributions. The resulting histogram of the nearest neighbour distances for both the experimental data sets and the randomly distributed data was normalized using the total number of NND calculated per ROI to calculate the percentage of the populate with distances smaller than a set threshold value.

Western Blotting

Cell lysates were extracted using RIPA buffer and 20 µg denatured protein per sample were loaded and separated using an 8% SDS-PAGE gel. Gels were run at 150 V for 2 hours and transferred into a nitrocellulose membrane (GE Healthcare) at 100 V for 1 hour. Following blocking with 5% milk (Sigma) in 0.1% TBS-T for 1 hour, membranes were incubated with

1:1000 dilution of antibodies against phosphorylated FAK (Tyr397, 3283, Cell Signalling, RRID:AB_2173659), phosphorylated ERK 1/2 (S217/221, 9154, Cell Signalling, RRID:AB_2138017), $P2Y_2$ (APR-010, Alomone Labs, RRID:AB_2040078), HSC 70 (SC7298, Santa Cruz, RRID:AB_627761) or α-tubulin (T5168, Sigma-Aldrich, RRID:AB_477579) with 5% BSA in 0.1% TBS-T overnight at 4ºC. Membranes were probed with anti-Mouse-HRP (P0447, DAKO, RRID:AB_2617137) or Anti-Rabbit-HRP (P0448, DAKO, RRID:AB_2617138) at 1:5000 in 5% milk in TBS-T for 1 hour at room temperature. Images were captured by using Luminata Forte Western HRP substrate (Millipore) and imaged with an Amersham Imager 600 (GE Healthcare).

Statistical analysis

For the statistical analysis of number and colocalisation of DNA-PAINT images, a minimum of five 4x4 μm^2 regions obtained from AsPC-1 cells were analysed per condition. For all experiments, normality tests were performed and the non-parametric Kruskal-Wallis test for significance was calculated. All graphs and statistical calculations of experimental data were made using Prism 9.4.1 (GraphPad).

References

Bailey, P. *et al.* (2016) 'Genomic analyses identify molecular subtypes of pancreatic cancer', *Nature*, 531, pp. 47–52. doi: 10.1038/nature16965.

Bao, L., Locovei, S. and Dahl, G. (2004) 'Pannexin membrane channels are mechanosensitive conduits for ATP', *Federation of European Biochemical Societies*, 572, pp. 65–68. doi: 10.1016/j.febslet.2004.07.009.

Bengtsson, A., Andersson, R. and Ansari, D. (2020) 'The actual 5-year survivors of pancreatic ductal adenocarcinoma based on real-world data', *Scientific Reports*, 10(16425).

737 doi: 10.1038/s41598-020-73525-y.

738 Boison, D. and Yegutkin, G. G. (2019) ‘Adenosine Metabolism : Emerging Concepts for
739 Cancer Therapy’, *Cancer Cell*, 36, pp. 582–596. doi: 10.1016/j.ccell.2019.10.007.

740 Bruns, R. F., Lu, G. H. and Pugsley, T. A. (1986) ‘Characterization of the A2 adenosine
741 receptor labeled by [3H]NECA in rat striatal membranes.’, *Molecular Pharmacology*, 29(4),
742 pp. 331–346.

743 Buffa, F. M. *et al.* (2010) ‘Large meta-analysis of multiple cancers reveals a common,
744 compact and highly prognostic hypoxia metagene’, *British Journal of Cancer*, 102(2), pp.
745 428–435. doi: 10.1038/sj.bjc.6605450.

746 Burnstock, G. and Novak, I. (2012) ‘Purinergic signalling in the pancreas in health and
747 disease’, *Journal of Endocrinology*, 213(2), pp. 123–141. doi: 10.1530/JOE-11-0434.

748 Calebiro, D. and Godbole, A. (2018) ‘Internalization of G-protein-coupled receptors :
749 Implication in receptor function , physiology and diseases’, *Best Practice & Research*
750 *Clinical Endocrinology & Metabolism*, 32, pp. 83–91. doi: 10.1016/j.beem.2018.01.004.

751 Chen, W. H. *et al.* (1982) ‘Human pancreatic adenocarcinoma: in vitro and in vivo
752 morphology of a new tumor line established from ascites.’, *In vitro*, 18(1), pp. 24–34. doi:
753 10.1007/BF02796382.

754 Chiarella, A. M. *et al.* (2021) ‘Extracellular ATP and Adenosine in Cancer Pathogenesis and
755 Treatment’, *Trends in Cancer*, 7(8), pp. 731–750. doi: 10.1016/j.trecan.2021.04.008.

756 Chorna, N. E. *et al.* (2007) ‘P2Y2 receptors induced cell surface redistribution of αv integrin
757 is required for activation of ERK 1/2 in U937 cells’, *Journal of Cellular Physiology*, 211(2),
758 pp. 410–422. doi: 10.1002/jcp.20946.

759 Collisson, E. A. *et al.* (2011) 'Subtypes of pancreatic ductal adenocarcinoma and their
760 differing responses to therapy', *Nature Medicine*, 17(4), pp. 500–504. doi:
761 10.1038/nm.2344.

762 Erb, L. *et al.* (2001) 'An RGD sequence in the P2Y2 receptor interacts with αvβ3 integrins
763 and is required for Go-mediated signal transduction', *Journal of Cell Biology*, 152(3), pp.
764 491–501. doi: 10.1083/jcb.152.3.491.

765 Feoktistov, I. *et al.* (2004) 'Hypoxia Modulates Adenosine Receptors in Human Endothelial
766 and Smooth Muscle Cells Toward an A 2B Angiogenic Phenotype', *Hypertension*, 44, pp.
767 649–654. doi: 10.1161/01.HYP.0000144800.21037.a5.

768 Fong, L. *et al.* (2020) 'Adenosine 2A receptor blockade as an immunotherapy for treatment-
769 refractory renal cell cancer', *Cancer Discovery*, 10(1), pp. 40–53. doi: 10.1158/2159-
770 8290.CD-19-0980.

771 Forrester, T. and Williams, C. A. (1977) 'Release of Adenosine Triphosphate from isolated
772 adult heart cells in response to hypoxia', *Journal of Physiology*, 268, pp. 371–390. doi:
773 10.1113/jphysiol.1977.sp011862.

774 Froeling, F. E. M. *et al.* (2009) 'Organotypic Culture Model of Pancreatic Cancer
775 Demonstrates that Stromal Cells Modulate E-Cadherin , beta-Catenin , and Ezrin
776 Expression in Tumor Cells', *The American Journal of Pathology*, 175(2), pp. 636–648. doi:
777 10.2353/ajpath.2009.090131.

778 Gao, J. *et al.* (2013) 'Integrative Analysis of Complex Cancer Genomics and Clinical
779 Profiles Using the cBioPortal Complementary Data Sources and Analysis Options', *Science
780 Signaling*, 6(269). doi: 10.1126/scisignal.2004088.

781 Ghandi, M. *et al.* (2019) 'Next-generation characterization of the Cancer Cell Line
782 Encyclopedia', *Nature*, 569, pp. 503–508. doi: 10.1038/s41586-019-1186-3.

783 Goedhart, J. and Luijsterburg, M. S. (2020) 'VolcaNoseR is a web app for creating,
784 exploring, labeling and sharing volcano plots', *Scientific Reports*, 10(20560). doi:
785 10.1038/s41598-020-76603-3.

786 Hu, L. P. *et al.* (2019) 'Targeting purinergic receptor P2Y2 prevents the growth of
787 pancreatic ductal adenocarcinoma by inhibiting cancer cell glycolysis', *Clinical Cancer*
788 *Research*, 25(4), pp. 1318–1330. doi: 10.1158/1078-0432.CCR-18-2297.

789 Ibuka, S. *et al.* (2015) 'The P2Y2 receptor promotes Wnt3a- and EGF-induced epithelial
790 tubular formation by IEC6 cells by binding to integrins', *Journal of Cell Science*, 128, pp.
791 2156–2168. doi: 10.1242/jcs.169060.

792 Jin, H. *et al.* (2014) 'P2Y2 receptor activation by nucleotides released from highly
793 metastatic breast cancer cells increases tumor growth and invasion via crosstalk with
794 endothelial cells', *Breast Cancer Research*, 16(R77). doi: 10.1186/bcr3694.

795 Joseph, M. D. *et al.* (2021) 'Quantitative super-resolution imaging for the analysis of GPCR
796 oligomerization', *Biomolecules*, 11(1503). doi: 10.3390/biom11101503.

797 Joseph, M. D. and Simoncelli, S. (2023) *qPAINT_pipeline*,
798 *Github*.https://github.com/Simoncelli-lab/qPAINT_pipeline. 25bcaf2.

799 Kadaba, R. *et al.* (2013) 'Imbalance of desmoplastic stromal cell numbers drives aggressive
800 cancer processes.', *The Journal of pathology*, 230(1), pp. 107–117. doi:
801 10.1002/path.4172.

802 Kapp, T. G. *et al.* (2017) 'A Comprehensive Evaluation of the Activity and Selectivity Profile
803 of Ligands for RGD-binding Integrins', *Scientific Reports*, 7(39805). doi:
804 10.1038/srep39805.

805 Karlsson, M. *et al.* (2021) 'A single–cell type transcriptomics map of human tissues',
806 *Science Advances*, 7(31), p. eabh2169. doi: 10.1126/sciadv.abh2169.

807 Ko, T. *et al.* (2012) 'P2Y receptors regulate proliferation of human pancreatic duct epithelial
808 cells', *Pancreas*, 41(5), pp. 797–803. doi: 10.1097/MPA.0b013e31823ba3b3.

809 Kocher, H. M. (2023) *Pancreatic Cancer*, *BMJ Best Practice bestpractice.bmj.com*.

810 Koong, A. C. *et al.* (2000) 'Pancreatic tumors show high levels of hypoxia', *International*
811 *Journal of Radiation Oncology Biology Physics*, 48(4), pp. 919–922. doi: 10.1016/S0360-
812 3016(00)00803-8.

813 Kurashima, Y. *et al.* (2012) 'Extracellular ATP mediates mast cell-dependent intestinal
814 inflammation through P2X7 purinoceptors', *Nature Communications*, 3(1034). doi:
815 10.1038/ncomms2023.

816 Kwon, J. A. E. H. *et al.* (2019) 'HIF-1α regulates A2B adenosine receptor expression in liver
817 cancer cells', *Experimental and Therapeutic Medicine*, 18, pp. 4231–4240. doi:
818 10.3892/etm.2019.8081.

819 Lánczky, A. and Győrffy, B. (2021) 'Web-Based Survival Analysis Tool Tailored for Medical
820 Research (KMplot): Development and Implementation', *Journal of Medical Interest*
821 *Research*, 23(7), p. e27633. doi: 10.2196/27633.

822 Lepzelter, D., Bates, O. and Zaman, M. (2012) 'Integrin Clustering in Two and Three
823 Dimensions', *Langmuir*, 28, pp. 5379–5386. doi: 10.1021/la203725a.

824 Li, W. *et al.* (2015) 'P2Y2 Receptor and EGFR Cooperate to Promote Prostate Cancer Cell
825 Invasion via ERK1/2 Pathway', *PLOS ONE*, 10(7), p. e0133165. doi:
826 10.1371/journal.pone.0133165.

827 Liao, Y. *et al.* (2019) 'WebGestalt 2019: gene set analysis toolkit with revamped UIs and
828 APIs', *Nucleic Acids Research*, 47, pp. 199–205. doi: 10.1093/nar/gkz401.

829 Livak, K. J. and Schmittgen, T. D. (2001) 'Analysis of Relative Gene Expression Data Using
830 Real-Time Quantitative PCR and the 2−ΔΔCT Method', *Methods*, 25(4), pp. 402–408. doi:
831 https://doi.org/10.1006/meth.2001.1262.

832 Lord, S. J. *et al.* (2020) 'SuperPlots: Communicating reproducibility and variability in cell
833 biology', *Journal of Cell Biology*, 219(6), p. e202001064. doi: 10.1083/JCB.202001064.

834 Love, M. I., Huber, W. and Anders, S. (2014) 'Moderated estimation of fold change and
835 dispersion for RNA-seq data with DESeq2', *Genome Biology*, 15(550). doi:
836 10.1186/s13059-014-0550-8.

837 Di Maggio, F. *et al.* (2016) 'Pancreatic stellate cells regulate blood vessel density in the
838 stroma of pancreatic ductal adenocarcinoma', *Pancreatology*. Elsevier India, a division of
839 Reed Elsevier India Pvt. Ltd, 16(6), pp. 995–1004. doi: 10.1016/j.pan.2016.05.393.

840 Martinez-Ramirez, A. S. *et al.* (2016) 'The P2RY2 Receptor Induces Carcinoma Cell
841 Migration and EMT Through Cross-Talk With Epidermal Growth Factor Receptor', *Journal
842 of Cellular Biochemistry*, 177, pp. 1016–1026. doi: 10.1002/jcb.25390.

843 Maurer, C. *et al.* (2019) 'Experimental microdissection enables functional harmonisation of
844 pancreatic cancer subtypes', *Gut*, 68, pp. 1034–1043. doi: 10.1136/gutjnl-2018-317706.

845 Moffitt, R. A. *et al.* (2015) 'Virtual microdissection identifies distinct tumor- and stroma-

specific subtypes of pancreatic ductal adenocarcinoma', *Nature Genetics*, 47(10). doi: 10.1038/ng.3398.

Muoboghare, M. O., Drummond, R. M. and Kennedy, C. (2019) 'Characterisation of P2Y2 receptors in human vascular endothelial cells using AR-C118925XX, a competitive and selective P2Y2 antagonist', *British Journal of Pharmacology*, 176(16), pp. 2894–2904. doi: 10.1111/bph.14715.

Murray, E. R. *et al.* (2022) 'Disruption of pancreatic stellate cell myofibroblast phenotype promotes pancreatic tumor invasion', *Cell Reports*, 38(110227). doi: 10.1016/j.celrep.2021.110227.

Neumann, A. *et al.* (2022) 'Discovery of P2Y2 Receptor Antagonist Scaffolds through Virtual High-Throughput Screening', *Journal of chemical information and modeling*, 62, pp. 1538–1549. doi: 10.1021/acs.jcim.1c01235.

Neuzillet, C. *et al.* (2017) 'Unravelling the pharmacologic opportunities and future directions for targeted therapies in gastro-intestinal cancers Part 1: GI carcinomas.', *Pharmacology & therapeutics*, 174, pp. 145–172. doi: 10.1016/j.pharmthera.2017.02.028.

Park, J. S. *et al.* (2020) 'Mechanical regulation of glycolysis via cytoskeleton architecture', *Nature*, 578, pp. 621–626. doi: 10.1038/s41586-020-1998-1.

Pellegatti, P. *et al.* (2008) 'Increased Level of Extracellular ATP at Tumor Sites : In Vivo Imaging with Plasma Membrane Luciferase', *PLOS ONE*, 3(7), p. e2599. doi: 10.1371/journal.pone.0002599.

Peng, X. L. *et al.* (2019) 'De novo compartment deconvolution and weight estimation of tumor samples using DECODER', *Nature Communications*, 10(4729). doi: 10.1038/s41467-

868 019-12517-7.

869 Pengo, T., Holden, S. J. and Manley, S. (2015) 'PALMsiever : a tool to turn raw data into
870 results for single-molecule localization microscopy', *Bioinformatics*, 31(5), pp. 797–798. doi:
871 10.1093/bioinformatics/btu720.

872 Ragnum, H. B. *et al.* (2015) 'The tumour hypoxia marker pimonidazole reflects a
873 transcriptional programme associated with aggressive prostate cancer', *British Journal of*
874 *Cancer*, 112, pp. 382–390. doi: 10.1038/bjc.2014.604.

875 Rahib, L. *et al.* (2021) 'Estimated Projection of US Cancer Incidence and Death to 2040',
876 *JAMA Network Open*, 4(4), p. e214708. doi: 10.1001/jamanetworkopen.2021.4708.

877 Riedl, J. *et al.* (2008) 'Lifeact : a versatile marker to visualize F-actin', *Nature Methods*, 5(7),
878 pp. 605–607. doi: 10.1038/NMETH.1220.

879 Schneider, E. *et al.* (2021) 'CD73-mediated adenosine production by CD8 T cell-derived
880 extracellular vesicles constitutes an intrinsic mechanism of immune suppression', *Nature*
881 *Communications*, 12(5911). doi: 10.1038/s41467-021-26134-w.

882 Schnitzbauer, J. *et al.* (2017) 'Super-resolution microscopy with DNA-PAINT', *Nature*
883 *Protocols*, 12(6), pp. 1198–1228. doi: 10.1038/nprot.2017.024.

884 Simoncelli, S. *et al.* (2020) 'Multi-color Molecular Visualization of Signaling Proteins
885 Reveals How C-Terminal Src Kinase Nanoclusters Regulate T Cell Receptor Activation',
886 *Cell Reports*, 33(108523). doi: 10.1016/j.celrep.2020.108523.

887 Strauss, S. and Jungmann, R. (2020) 'Up to 100-fold speed-up and multiplexing in
888 optimized DNA-PAINT', *Nature Methods*, 17, pp. 789–791. doi: 10.1038/s41592-020-0869-
889 x.

890 Synnestvedt, K. *et al.* (2002) 'Ecto-5′-nucleotidase (CD73) regulation by hypoxia-inducible
891 factor-1 mediates permeability changes in intestinal epithelia', *Journal of Clinical*
892 *Investigation*, 110(7), pp. 993–1002. doi: 10.1172/JCI15337.

893 Tak, E. *et al.* (2016) 'Upregulation of P2Y2 nucleotide receptor in human hepatocellular
894 carcinoma cells', *Journal of International Medical Research*, 44(6), pp. 1234–1247. doi:
895 10.1177/0300060516662135.

896 Tan, M. H. *et al.* (1986) 'Characterization of a New Primary Human Pancreatic Tumor Line',
897 *Cancer Investigation*. Taylor & Francis, 4(1), pp. 15–23. doi: 10.3109/07357908609039823.

898 Tan, Y. H. *et al.* (2008) 'A Nanoengineering Approach for Immobilization', *ACS Nano*, 2(11),
899 pp. 2374–2384. doi: 10.1021/nn800508f.

900 Tang, Z. *et al.* (2017) 'GEPIA : a web server for cancer and normal gene expression
901 profiling and interactive analyses', *Nucleic Acids Research*, 45, pp. W98–W102. doi:
902 10.1093/nar/gkx247.

903 Teoh, C. M. *et al.* (2012) 'Integrin and GPCR Crosstalk in the Regulation of ASM
904 Contraction Signaling in Asthma', *Journal of Allergy*, 2012(341282). doi:
905 10.1155/2012/341282.

906 Tulapurkar, M. E. *et al.* (2005) 'Endocytosis mechanism of P2Y2 nucleotide receptor tagged
907 with green fluorescent protein: Clathrin and actin cytoskeleton dependence', *Cellular and*
908 *Molecular Life Sciences*, 62, pp. 1388–1399. doi: 10.1007/s00018-005-5052-0.

909 Varet, H. *et al.* (2016) 'SARTools: A DESeq2- and EdgeR-Based R Pipeline for
910 Comprehensive Differential Analysis of RNA-Seq Data', *PLoS ONE*, 11(6), p. e0157022.
911 doi: 10.1371/journal.pone.0157022.

Di Virgilio, F. *et al.* (2018) 'Extracellular ATP and P2 purinergic signalling in the tumour microenvironment', *Nature Reviews Cancer*, 18, pp. 601–618. doi: 10.1038/s41568-018-0037-0.

Wang, Q. *et al.* (2020) 'Mitochondrial Protein UQCRC1 is Oncogenic and a Potential Therapeutic Target for Pancreatic Cancer', *Theranostics*, 10(5), pp. 2141–57. doi: 10.7150/thno.38704.

Wang, T. *et al.* (2005) 'CD97 , an adhesion receptor on inflammatory cells , stimulates angiogenesis through binding integrin counterreceptors on endothelial cells', *Blood*, 105(7), pp. 2836–2844. doi: 10.1182/blood-2004-07-2878.

Winter, S. C. *et al.* (2007) 'Relation of a Hypoxia Metagene Derived from Head and Neck Cancer to Prognosis of Multiple Cancers', *Cancer Research*, 67(7), pp. 3441–3449. doi: 10.1158/0008-5472.CAN-06-3322.

Xing, S. *et al.* (2016) 'Modeling Interactions among Individual P2 Receptors to Explain Complex Response Patterns over a Wide Range of ATP Concentrations', *Frontiers in Physiology*, 7(294). doi: 10.3389/fphys.2016.00294.

Yu, X. *et al.* (2021) 'CD73 induces gemcitabine resistance in pancreatic ductal adenocarcinoma: A promising target with non-canonical mechanisms', *Cancer Letters*, 519, pp. 289–303. doi: 10.1016/j.canlet.2021.07.024.

Yuen, A. and Diaz, B. (2014) 'The impact of hypoxia in pancreatic cancer invasion and metastasis', *Hypoxia*, 2, pp. 91–106. doi: 10.2147/HP.S52636.

Acknowledgments

We thank the Barts Pancreatic Tissue Bank (BPTB) for providing pancreatic tissue slides presented in this work. BPTB is supported by Pancreatic Cancer Research Fund and we thank all its members, in particular, Prof. Claude Chelala, Christine Hughes, Ahmet Imrali and Amina Hughes for help, as well as Consultant Pathologist Dr Joanne Chin-Aleong and members of Tissue Access Committee and Operations Group. We thank Dr Ann-Marie Baker for her expertise on RNAscope experiments. This work was supported by a Medical Research Council (MRC) iCase award to P.J.M. and R.P.G. from Barts Charity and the MRC Doctoral Training Programme for E.T.B. at Queen Mary University of London (Project MRC0227). N.J.R. acknowledges the QMUL MRC Doctoral Training Program (MR/N014308/1). M.D.J. acknowledges support from the BBSRC (BB/T008709/1) via the London Interdisciplinary Doctoral Programme and S.S. acknowledges financial support from the Royal Society through a Dorothy Hodgkin fellowship (DHF\R1\191019) and a Research Grant (RGS\R2\202038). This work was supported by Cancer Research UK (CRUK) awarded to E.P.C. and R.P.G. (A27781) and a CRUK Centre grant to Barts Cancer Institute (A25137). Diagrams were generated using BioRender.

Data availability

Human PDAC tumour data were generated by TCGA Research Network (https://www.cancer.gov/tcga) and by the Clinical Proteomic Tumour Analysis Consortium (https://www.proteomics.cancer.gov). The Genotype-Tissue Expression (GTEx) Project was used for the analysis of normal pancreatic tissue samples (https://gtexportal.org).

Conflict of Interest

The authors declare that they have no conflict of interest.

Figure 1. Characterisation of purinergic signalling in pancreatic adenocarcinoma. A Purinergic signalling proteins and gene names. **B** Hazard ratios of overall survival calculated using KMPlot and the PAAD TCGA cohort (n=177) for different purinergic genes. Statistically significant hazard ratios (log rank p-value) are highlighted in red for worse survival and in blue for better survival. **C** Heatmap of purinergic genes significantly correlated ($q < 0.05$) to high (purple) or low (light blue) Winter hypoxia scores in the PAAD TCGA data set. Overall survival status and overall survival in months is shown at the top, and samples are ranked using the Winter Hypoxia score (Generated with cBioPortal). **D** Differential expression analysis of 60 paired stromal and tumour tissue microdissections (GSE93326) showing significantly differentially expressed purinergic genes in stromal or tumour epithelial tissue. **E** Gene weights for purinergic genes representing the relevance of each gene to each cell type compartment, obtained from DECODER PDAC TCGA deconvolution analysis.

Figure 1-figure supplement 1. Characterisation of purinergic genes in pancreatic adenocarcinoma. A Oncoprint from the PAAD TCGA cohort generated using cBioPortal. mRNA high and mRNA low represent Z-score values of >1 or <-1.**B** KMplot generated in cBioPortal for patients with high (red) vs low (blue) Winter hypoxia scores **C** Volcano plots for differential expression results of PAAD TCGA patient of high or low hypoxia scores using 3 different hypoxia signatures (Winter, Ragnum and Buffa). **D** Heat map of purinergic mRNA expression data for different PDAC cell lines from CCLE. **E** Comparison of normal versus tumour normalised transcripts per million (TPM) expression of purinergic genes. Data obtained using GEPIA and PAAD TCGA and GTEx.

Figure 2. Expression of $P2Y_2$ is specific to cancer cells, correlated with decreased overall survival in patients and drives cytoskeletal rearrangements. A RNAscope *in-situ* hybridisation of $P2Y_2$ mRNA expression (magenta) in tumour and matching normal adjacent tissue. **B** $P2Y_2$ mRNA expression in tumour (TCGA) and normal (GTEx) pancreatic tissue samples (* p <0.0001). Graph generated using GEPIA. **C** Kaplan-Meier plot comparing patients with high vs low expression of $P2Y_2$ in the PAAD TCGA cohort. Graph generated using KMplot. **D** Top result of a GSEA (performed with WebGestalt) of two different pancreatic adenocarcinoma patient cohorts (PAAD TCGA and PDAC CPTAC) for the PANTHER pathway functional database. **E** Incucyte images of the pancreatic cancer cell line AsPC-1 12 hours after treatment with 100 μM ATP alone or with 5 μM AR-C ($P2Y_2$ antagonist). Cells are transduced with Lifeact to visualise f-actin (green). **F** Schematic of the amino acid sequence of $P2Y_2$ showing an RGD motif in the first extracellular loop (image generated in gpcrdb.org). **G** IF staining of $P2Y_2$ (green), integrin αV (red) and DAPI (blue) in AsPC-1 cells showing colocalisation of $P2Y_2$ and integrin αV (yellow).

Figure 2-figure supplement 1. mRNA and protein expression of $P2Y_2$ in PDAC cells. A RNAscope *in-situ* hybridisation of a positive control (*PPIB*, Cyclophilin B), negative control (*DapB*) and $P2Y_2$ mRNA expression in a PDAC tissue slide showing tumour and normal adjacent tissue. **B** Single cell expression of $P2Y_2$ in health pancreatic tissue from the Human Protein Atlas (https://www.proteinatlas.org/ENSG00000175591-P2RY2/single+cell+type/pancreas). **C** Top 4 results of a GSEA (performed with WebGestalt) of two different pancreatic adenocarcinoma patient cohorts (PAAD TCGA and PDAC CPTAC) for the 'Molecular Function' Gene Ontology (GO) functional database**. D** Incucyte analysis of average object area related to the average cell area of AsPC-1 cells at different concentrations of ATP. **E** Incucyte images of AsPC-1 cells with different

concentrations of AR-C with or without ATP.**F** IF staining of 4 different PDAC cell lines showing various levels of $P2Y_2$ (green) and integrin αV (red) protein expression. **G** The respective reads per kilobase of exon per million reads mapped (RPKM) from CCLE.

Figure 3. The RGD motif in $P2Y_2$ is required for extracellular ATP-driven cancer cell invasion. A Schematic diagram of the hanging drop sphere model for 3D sphere invasion assays. **B** Brightfield and fluorescent images of spheres formed using AsPC-1 cells (magenta) with a histone 2B (H2B) tagged with red fluorescent protein (RFP) and the stellate cell line PS-1 (green) with H2B tagged with a green fluorescent protein (GFP). Middle pannel shows AsPC-1 cells in spheres with a dotted line highlighting the central sphere area. Spheres were treated with vehicle control or 100 μM ATP alone or with 5 μM AR-C or 10 μM cRGDfV. The quantification is shown in **C** using SuperPlots, where each colour represents a biological repeat (*n* = 3) and the larger points represent the mean % Invasion for each repeat. **D** Quantification of spheres formed by AsPC-1 cells transfected with a control siRNA or $P2Y_2$ siRNA and treated with or without 100 μM ATP. **E** Brightfield and fluorescent images of spheres formed by AsPC-1 cells subjected to CRISPR/Cas9 gene disruption using a control guide RNA (CTR^{CRISPR}) or $P2Y_2$ guide RNAs ($P2Y_2^{CRISPR}$) and treated with or without 100 μM ATP**.** Quantification in **F**. **G, I** Brightfield and fluorescent images of AsPC-1 $P2Y_2^{CRISPR}$ cells or PANC-1 cells (respectively) transfected with wild-type *P2RY2* ($P2Y_2^{RGD}$) or mutant *P2RY2*^{D97E} ($P2Y_2^{RGE}$) treated with or without 100 μM ATP and its quantification in **H** and **J**, respectively. Statistical analysis with Kuskal-Wallis multiple comparison test.

Figure 3-figure supplement 1. Invasion and migration experiments in PDAC cell lines. A Hanging drop sphere with and without PS-1 cells. **B, C** Quantification of AsPC-1 spheres treated with 100 μM UTP or ATPγS (respectively) in absence or together with 5 μM AR-C or 10 μM cRGDfV (*n* = 3 biological replicates). **D** IF staining of $P2Y_2$ in AsPC-1 and PS-1 stellate cells. **E** Migration assay with AsPC-1 and 100 μM ATP in absence or together with 5 μM AR-C or/and 10 μM cRGDfV and **F** its quantification (*n* = 3 biological replicates). **G** 3D sphere invasion assay using BxPC-3 cells treated with 100 μM of ATP in absence or together with 5 μM AR-C or/and 10 μM cRGDfV and **H** its quantification (*n* = 3 biological replicates). **I** qPCR of $P2Y_2$ expression and western blot of siRNA treated cells (control siRNA and $P2Y_2$ targeting siRNA, *n* = 3 biological replicates). **J** AsPC-1 $P2Y_2^{CRISPR}$ spheres treated with or without 5 μM of AR-C (*n* = 3 biological replicates). **K** $P2Y_2$ IF staining of AsPC-1 $P2Y_2^{CRISPR}$ cells transfected with an empty vector, $P2Y_2^{RGD}$ or $P2Y_2^{RGE}$ plasmids.

Figure 3-figure supplement 1-source data 1. Labelled uncropped blot of Figure 3-supplemen 1 I.

Figure 3-figure supplement 1-source data 2. Full unedited blot of Figure 3-supplement 1 I.

Figure 4. DNA-PAINT super-resolution microscopy reveals ATP and RGD-dependent changes in number and distribution of integrin αV and $P2Y_2$ molecules in the plasma membrane. A, B Overview of the DNA-PAINT microscopy technique and qPAINT analysis pipeline**. C** Histogram of qPAINT indices for αV (blue) and $P2Y_2$ (red) single molecule localisation clusters. Solid lines represent multi-peak Gaussian fit. **D** Rendered DNA-PAINT images of AsPC-1 $P2Y_2^{CRISPR}$ cells transfected with $P2Y_2^{RGD}$ or $P2Y_2^{RGE}$ with or without 100

μM of ATP and close ups showing the protein maps reconstructed from DNA-PAINT localization maps of $P2Y_2$ (red) and integrin αV (cyan). The quantification of the number of proteins or protein clusters (>3 proteins) in each region of interest (ROI) are for $P2Y_2$ (red)(**E** and **F** respectively) and integrin αV (cyan) (**G** and **H** respectively). Quantification of protein proximity using the nearest neighbour distance (NND), with the percentages of integrin αV and $P2Y_2$ proteins being < 50 nm apart (**I**), between different αV integrins being 20-100 nm (**J**) or < 20 nm (**K**) apart; and $P2Y_2$ from other $P2Y_2$ proteins being < 40 nm apart (**H**). Statistical analysis with Kuskal-Wallis multiple comparison test.

Figure 4-figure supplement 1. Quantification of P2Y2 and integrin αV at the membrane using DNA-PAINT. A, B, C, D Normal AsPC-1 cells (untransfected and unchanged $P2Y_2$ expression) treated with vehicle control or 100 μM of ATP with or without cRGDfV were imaged with DNA-PAINT. The quantification of the number of proteins or protein clusters (>3 proteins) in each region of interest (ROI) are shown in red for $P2Y_2$ and in cyan for integrin αV E, F Percentage of integrin αV and $P2Y_2$ in clusters normalised to the number of proteins (integrin αV or $P2Y_2$ proteins respectively) in AsPC-1 $P2Y_2^{CRISPR}$ cells transfected with $P2Y_2^{RGD}$ or $P2Y_2^{RGE}$ and treated with vehicle control or 100 μM of ATP**.**

Figure 4-figure supplement 2. Schematic diagram of NND distances and NND histograms A Schematic diagram of the predicted maximum distance between fluorescent molecules indicating physical contact between proteins, to the nearest first significant figure. **B** Histograms of the nearest neighbour distance between proteins vs the frequency of occurrence for AsPC-1 $P2Y_2^{CRISPR}$ in different conditions (solid line, strong colour) or randomly computer-generated controls (dotted line, light colour).

Figure 5. The RGD motif in $P2Y_2$ is involved in FAK/ERK signalling. A ,**B,** Western blots of phosphorylated FAK (p-FAK) and ERK (p-ERK) of AsPC-1 cells treated with ATP or pre-treated for 30 min with AR-C (5 μM) or cRGDfV (10 μM), respectively and treated with ATP for 60 min. **C** Western blot of AsPC-1 $P2Y_2^{CRISPR}$ cells transfected with $P2Y_2^{RGD}$ or $P2Y_2^{RGE}$ and treated with ATP for 60 min. Representative images of three biological replicates.

Figure 5-source data 1. Labelled uncropped blots of Figure 5.

Figure 5-source data 2. Full unedited blots of Figure 5.

Figure 6. Proposed mechanism of $P2Y_2$ and integrin interactions in pancreatic cancer invasion.

Supplementary File 1. Pancreatic cancer molecular subtypes associated with purinergic gene expressions. Purinergic genes with significantly higher expression in a specific molecular subtype have been listed bellow. If no significant higher expression was observed not applicable (N/A) is shown.

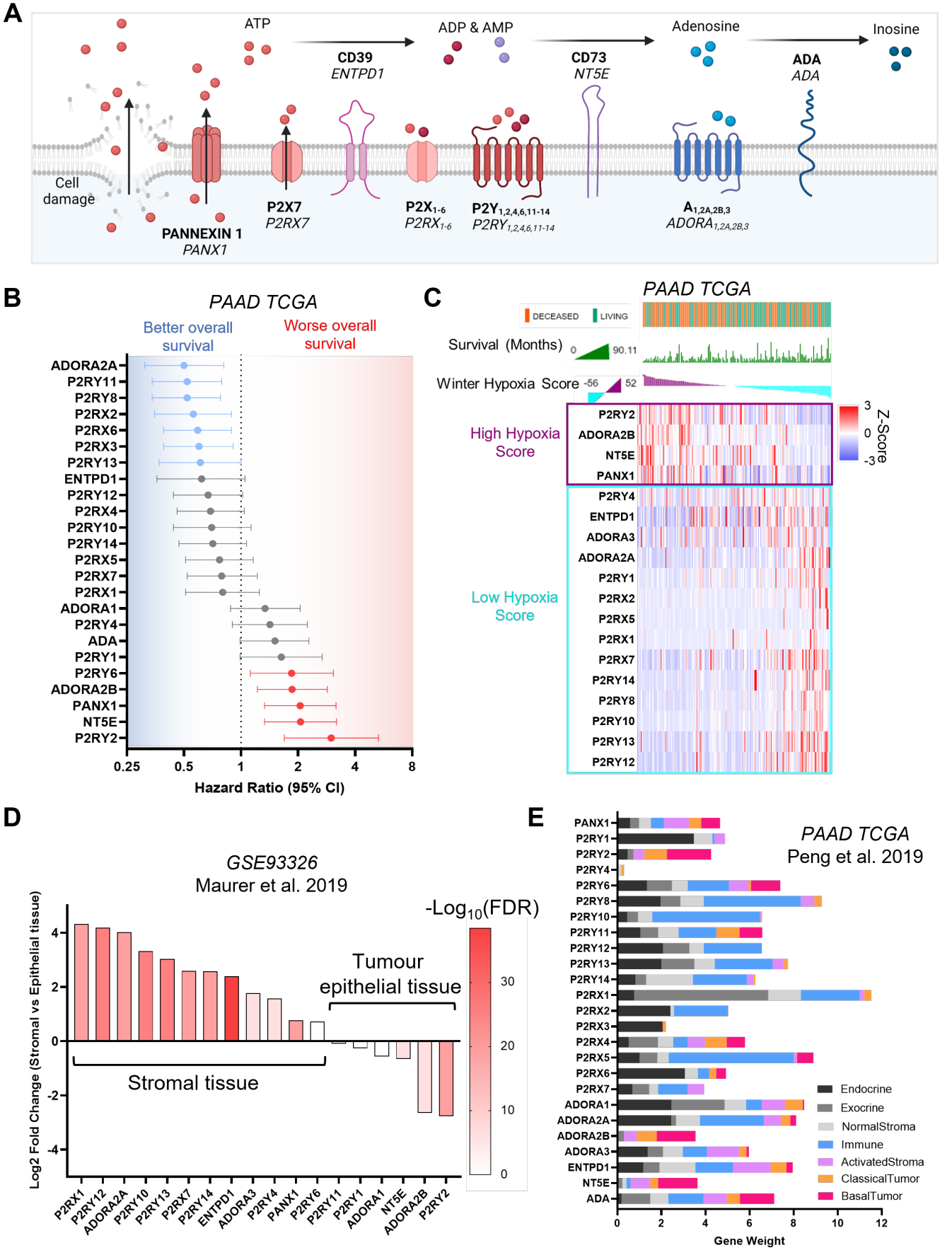
A
ATP
CD39
ENTPD1
ADP & AMP
CD73
NT5E
Adenosine
ADA
ADA
Inosine
Cell damage
PANNEXIN 1
PANX1
P2X7
P2RX7
P2X1-6
P2RX1-6
P2Y1,2,4,6,11-14
P2RY1,2,4,6,11-14
A1,2A,2B,3
ADORA1,2A,2B,3
B
PAAD TCGA
Better overall survival
Worse overall survival
ADORA2A
P2RY11
P2RY8
P2RX2
P2RX6
P2RX3
P2RY13
ENTPD1
P2RY12
P2RX4
P2RY10
P2RY14
P2RX5
P2RX7
P2RX1
ADORA1
P2RY4
ADA
P2RY1
P2RY6
ADORA2B
PANX1
NT5E
P2RY2
0.25
0.5
1
2
4
8
Hazard Ratio (95% CI)
C
PAAD TCGA
DECEASED
LIVING
Survival (Months)
0
90.11
Winter Hypoxia Score
-56
52
High Hypoxia Score
P2RY2
ADORA2B
NT5E
PANX1
Low Hypoxia Score
P2RY4
ENTPD1
ADORA3
ADORA2A
P2RY1
P2RX2
P2RX5
P2RX1
P2RX7
P2RY14
P2RY8
P2RY10
P2RY13
P2RY12
3
0
-3
Z-Score
D
GSE93326
Maurer et al. 2019
-Log10(FDR)
Tumour epithelial tissue
Stromal tissue
Log2 Fold Change (Stromal vs Epithelial tissue)
4
2
0
-2
-4
30
20
10
0
P2RX1
P2RY12
ADORA2A
P2RY10
P2RY13
P2RX7
P2RY14
ENTPD1
ADORA3
P2RY4
PANX1
P2RY6
P2RY11
P2RY1
ADORA1
NT5E
ADORA2B
P2RY2
E
PAAD TCGA
Peng et al. 2019
PANX1
P2RY1
P2RY2
P2RY4
P2RY6
P2RY8
P2RY10
P2RY11
P2RY12
P2RY13
P2RY14
P2RX1
P2RX2
P2RX3
P2RX4
P2RX5
P2RX6
P2RX7
ADORA1
ADORA2A
ADORA2B
ADORA3
ENTPD1
NT5E
ADA
Endocrine
Exocrine
NormalStroma
Immune
ActivatedStroma
ClassicalTumor
BasalTumor
0
2
4
6
8
10
12
Gene Weight

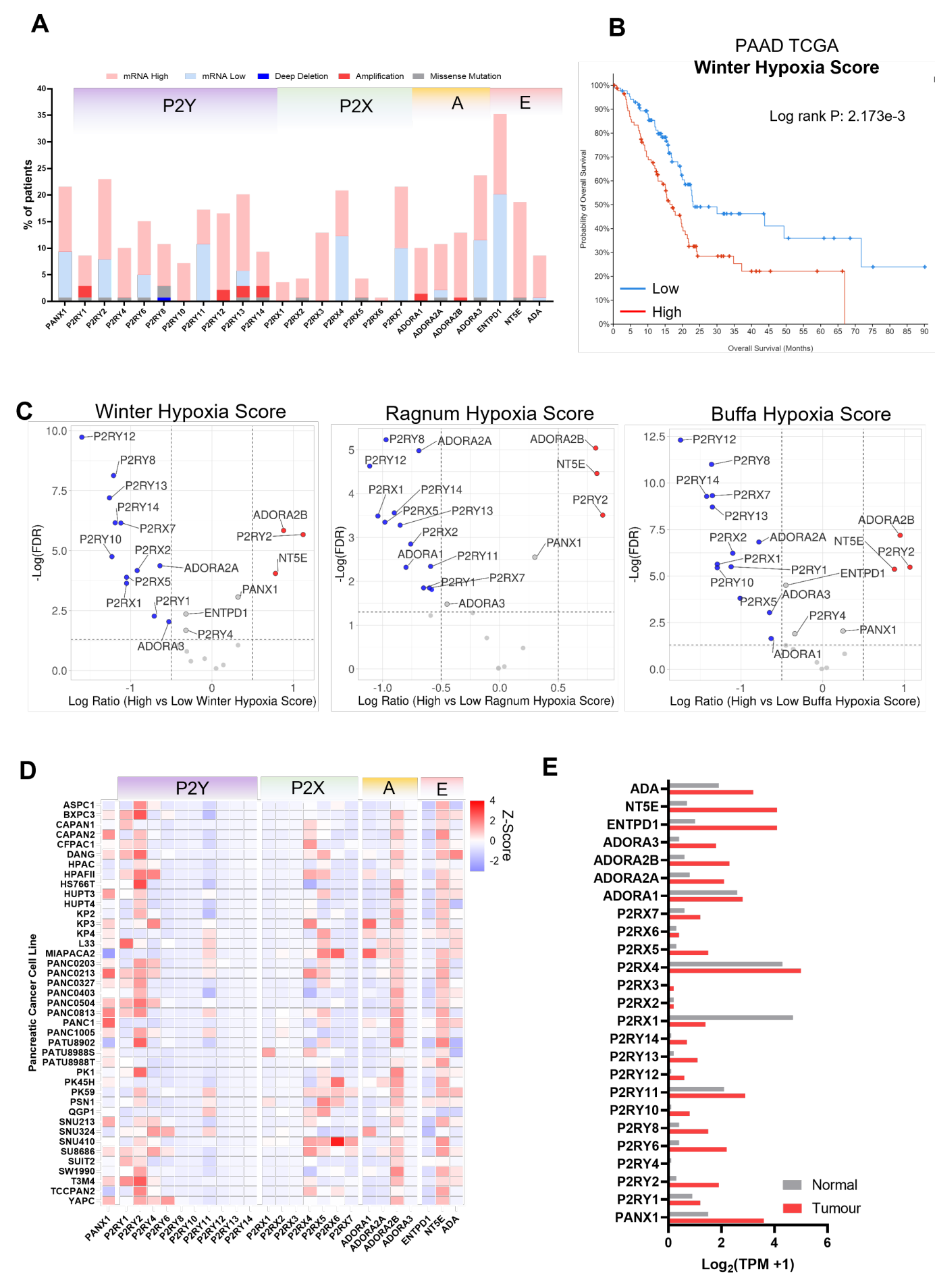
A
mRNA High
mRNA Low
Deep Deletion
Amplification
Missense Mutation
P2Y
P2X
A
E
% of patients
PANX1 P2RY1 P2RY2 P2RY4 P2RY6 P2RY8 P2RY10 P2RY11 P2RY12 P2RY13 P2RY14 P2RX1 P2RX2 P2RX3 P2RX4 P2RX5 P2RX6 P2RX7 ADORA1 ADORA2A ADORA2B ADORA3 ENTPD1 NT5E ADA
B
PAAD TCGA
Winter Hypoxia Score
Log rank P: 2.173e-3
Probability of Overall Survival
Low
High
Overall Survival (Months)
C
Winter Hypoxia Score
Ragnum Hypoxia Score
Buffa Hypoxia Score
-Log(FDR)
Log Ratio (High vs Low Winter Hypoxia Score)
Log Ratio (High vs Low Ragnum Hypoxia Score)
Log Ratio (High vs Low Buffa Hypoxia Score)
D
P2Y
P2X
A
E
Z-Score
Pancreatic Cancer Cell Line
ASPC1 BXPC3 CAPAN1 CAPAN2 CFPAC1 DANG HPAC HPAFII HS766T HUPT3 HUPT4 KP2 KP3 KP4 L33 MIAPACA2 PANC0203 PANC0213 PANC0327 PANC0403 PANC0504 PANC0813 PANC1 PANC1005 PATU8902 PATU8988S PATU8988T PK1 PK45H PK59 PSN1 QGP1 SNU213 SNU324 SNU410 SU8686 SUIT2 SW1990 T3M4 TCCPAN2 YAPC
E
ADA NT5E ENTPD1 ADORA3 ADORA2B ADORA2A ADORA1 P2RX7 P2RX6 P2RX5 P2RX4 P2RX3 P2RX2 P2RX1 P2RY14 P2RY13 P2RY12 P2RY11 P2RY10 P2RY8 P2RY6 P2RY4 P2RY2 P2RY1 PANX1
Normal
Tumour
Log2(TPM +1)

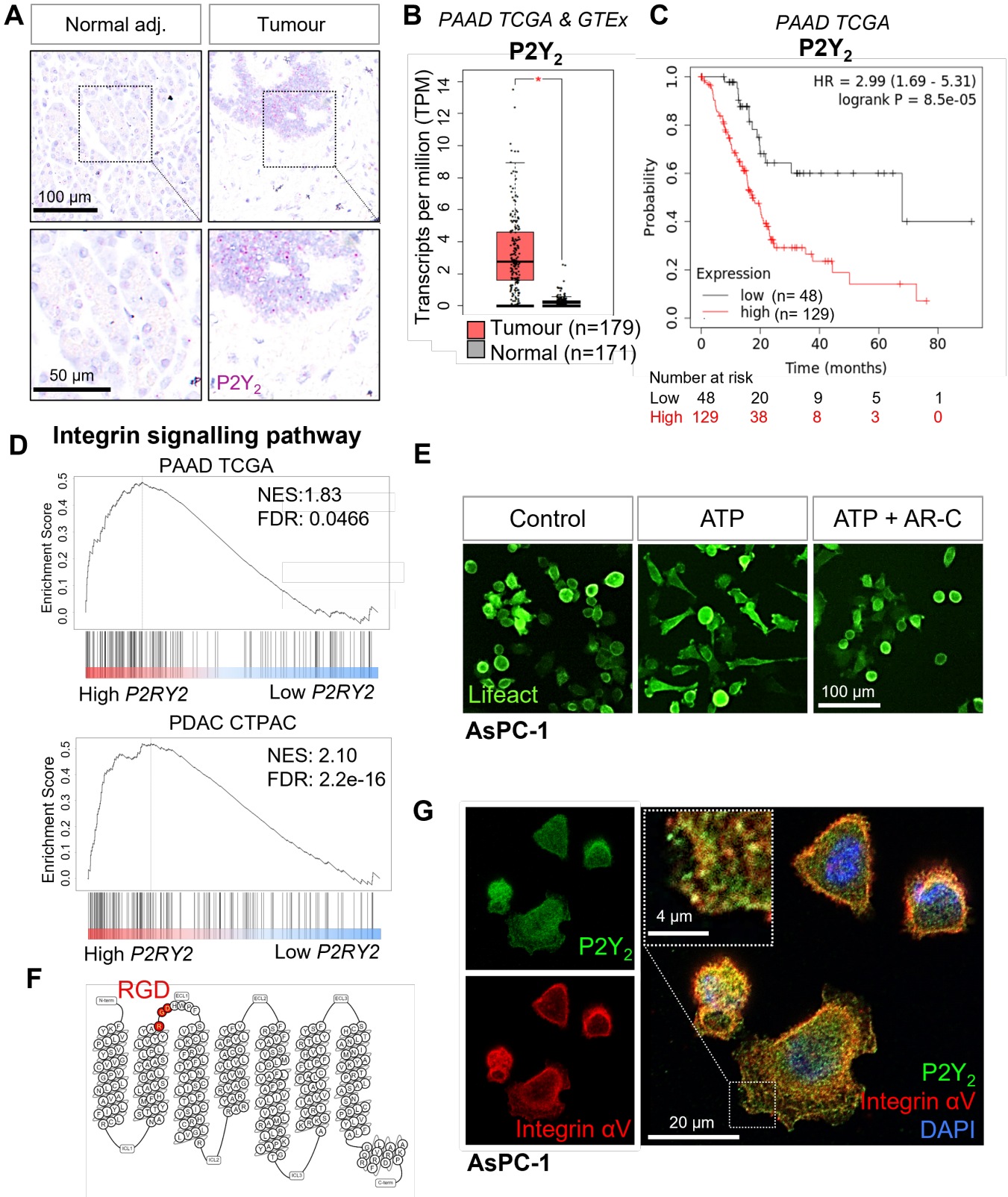
A
Normal adj.
Tumour
100 µm
50 µm
P2Y2
B
PAAD TCGA & GTEx
P2Y2
Transcripts per million (TPM)
Tumour (n=179)
Normal (n=171)
C
PAAD TCGA
P2Y2
HR = 2.99 (1.69 - 5.31)
logrank P = 8.5e-05
Probability
Expression
low (n= 48)
high (n= 129)
Time (months)
Number at risk
Low 48 20 9 5 1
High 129 38 8 3 0
D
Integrin signalling pathway
PAAD TCGA
NES:1.83
FDR: 0.0466
Enrichment Score
High P2RY2
Low P2RY2
PDAC CTPAC
NES: 2.10
FDR: 2.2e-16
Enrichment Score
High P2RY2
Low P2RY2
E
Control
ATP
ATP + AR-C
Lifeact
100 µm
AsPC-1
F
RGD
G
P2Y2
Integrin αV
4 µm
20 µm
P2Y2
Integrin αV
DAPI
AsPC-1

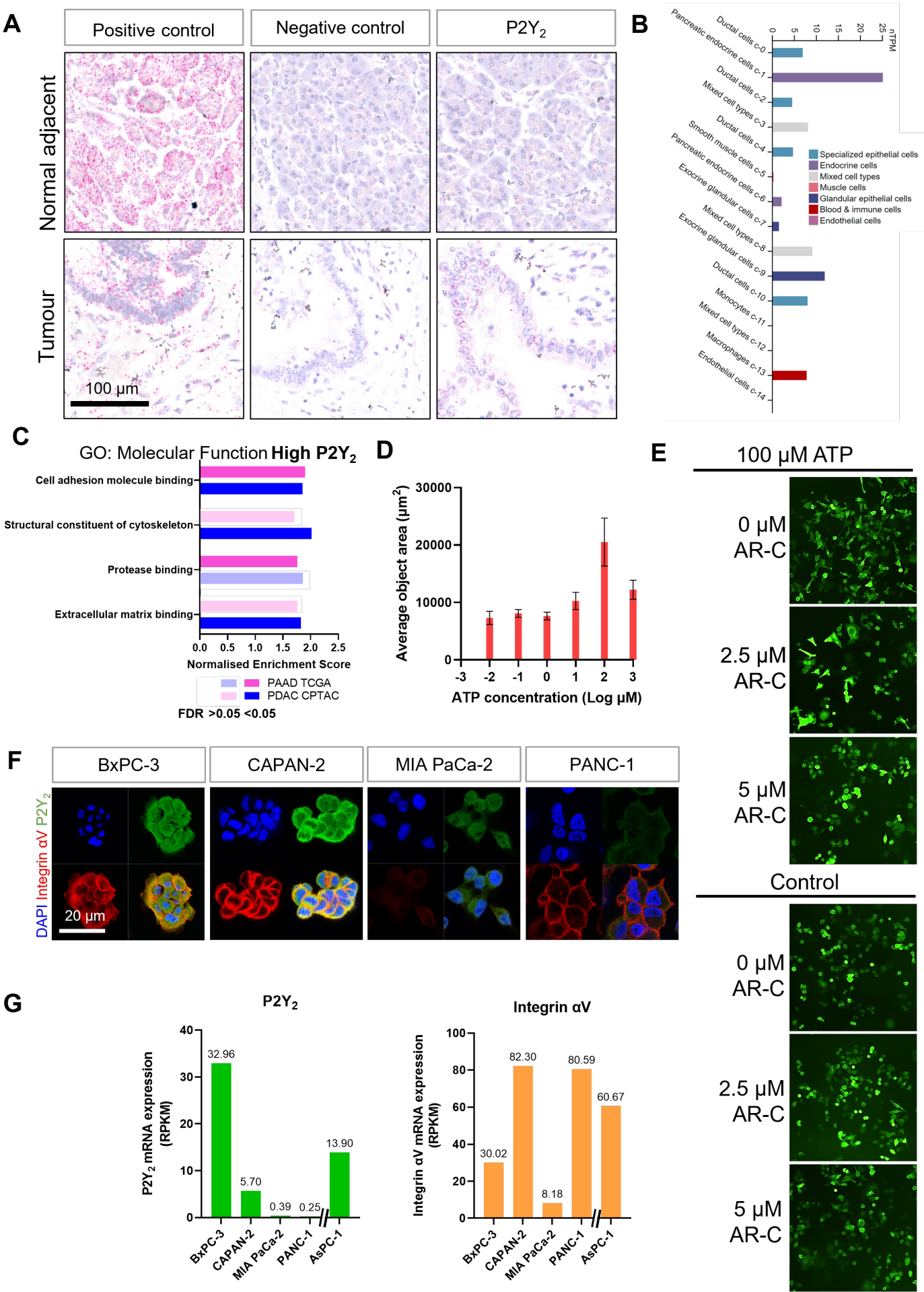
A
Positive control
Negative control
P2Y2
Normal adjacent
Tumour
100 µm
B
nTPM
Ductal cells c-0
Pancreatic endocrine cells c-1
Ductal cells c-2
Mixed cell types c-3
Ductal cells c-4
Smooth muscle cells c-5
Pancreatic endocrine cells c-6
Exocrine glandular cells c-7
Mixed cell types c-8
Exocrine glandular cells c-9
Ductal cells c-10
Monocytes c-11
Mixed cell types c-12
Macrophages c-13
Endothelial cells c-14
Specialized epithelial cells
Endocrine cells
Mixed cell types
Muscle cells
Glandular epithelial cells
Blood & immune cells
Endothelial cells
C
GO: Molecular Function High P2Y2
Cell adhesion molecule binding
Structural constituent of cytoskeleton
Protease binding
Extracellular matrix binding
Normalised Enrichment Score
PAAD TCGA
PDAC CPTAC
FDR >0.05 <0.05
D
Average object area (µm2)
ATP concentration (Log µM)
E
100 µM ATP
0 µM AR-C
2.5 µM AR-C
5 µM AR-C
Control
0 µM AR-C
2.5 µM AR-C
5 µM AR-C
F
BxPC-3
CAPAN-2
MIA PaCa-2
PANC-1
DAPI Integrin αV P2Y2
20 µm
G
P2Y2
P2Y2 mRNA expression (RPKM)
32.96
5.70
0.39
0.25
13.90
Integrin αV
Integrin αV mRNA expression (RPKM)
30.02
82.30
8.18
80.59
60.67
BxPC-3
CAPAN-2
MIA PaCa-2
PANC-1
AsPC-1

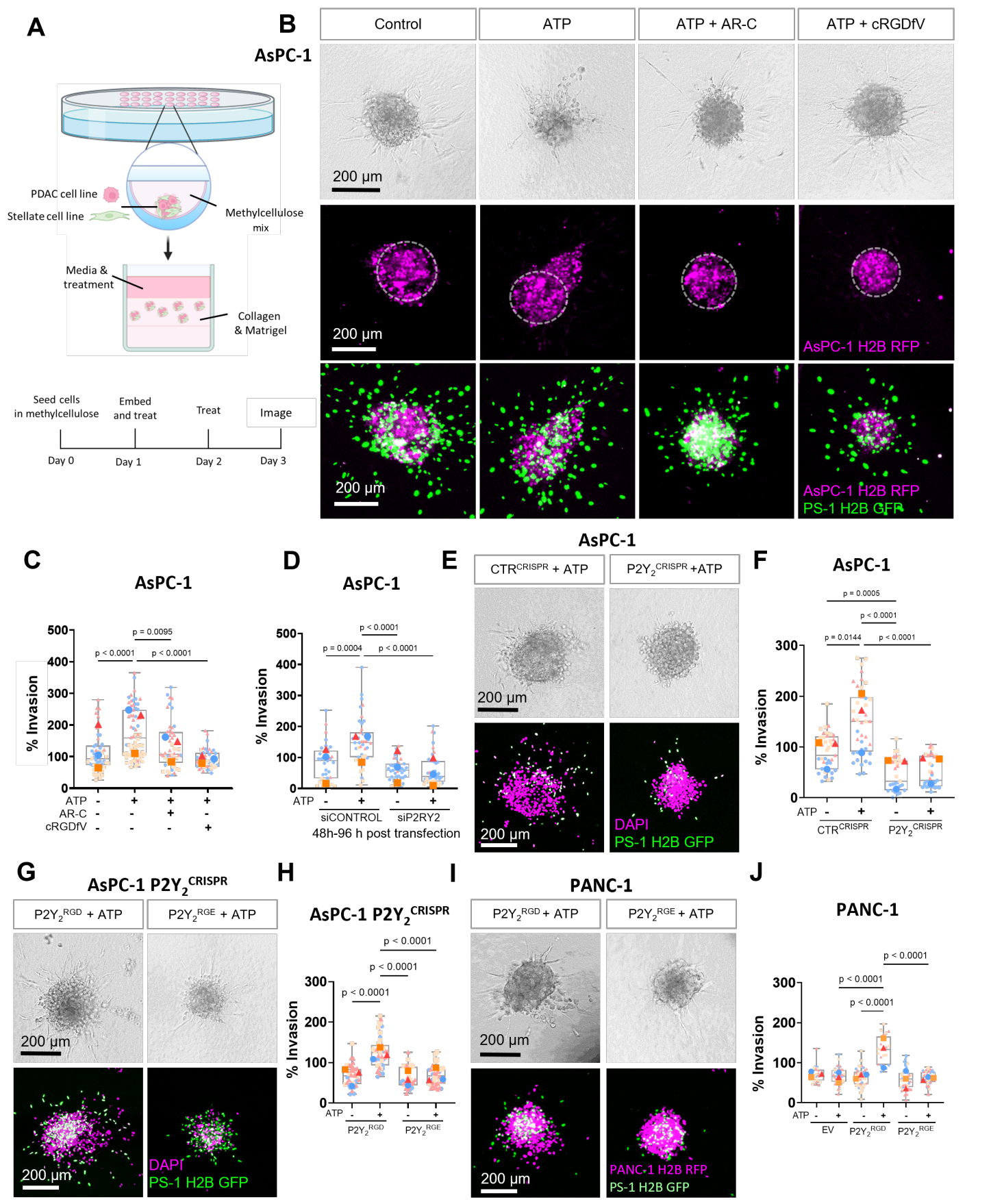
A
B
AsPC-1
Control
ATP
ATP + AR-C
ATP + cRGDfV
PDAC cell line
Stellate cell line
Methylcellulose mix
Media & treatment
Collagen & Matrigel
Seed cells in methylcellulose
Embed and treat
Treat
Image
Day 0
Day 1
Day 2
Day 3
200 µm
AsPC-1 H2B RFP
PS-1 H2B GFP
C
AsPC-1
% Invasion
p = 0.0095
p < 0.0001
p < 0.0001
ATP
AR-C
cRGDfV
D
AsPC-1
p < 0.0001
p = 0.0004
p < 0.0001
siCONTROL
siP2RY2
48h-96 h post transfection
E
AsPC-1
CTR CRISPR + ATP
P2Y2 CRISPR +ATP
DAPI
F
AsPC-1
p = 0.0005
p < 0.0001
p = 0.0144
p < 0.0001
CTR CRISPR
P2Y2 CRISPR
G
AsPC-1 P2Y2 CRISPR
P2Y2 RGD + ATP
P2Y2 RGE + ATP
H
AsPC-1 P2Y2 CRISPR
I
PANC-1
J
PANC-1
p < 0.0001
EV

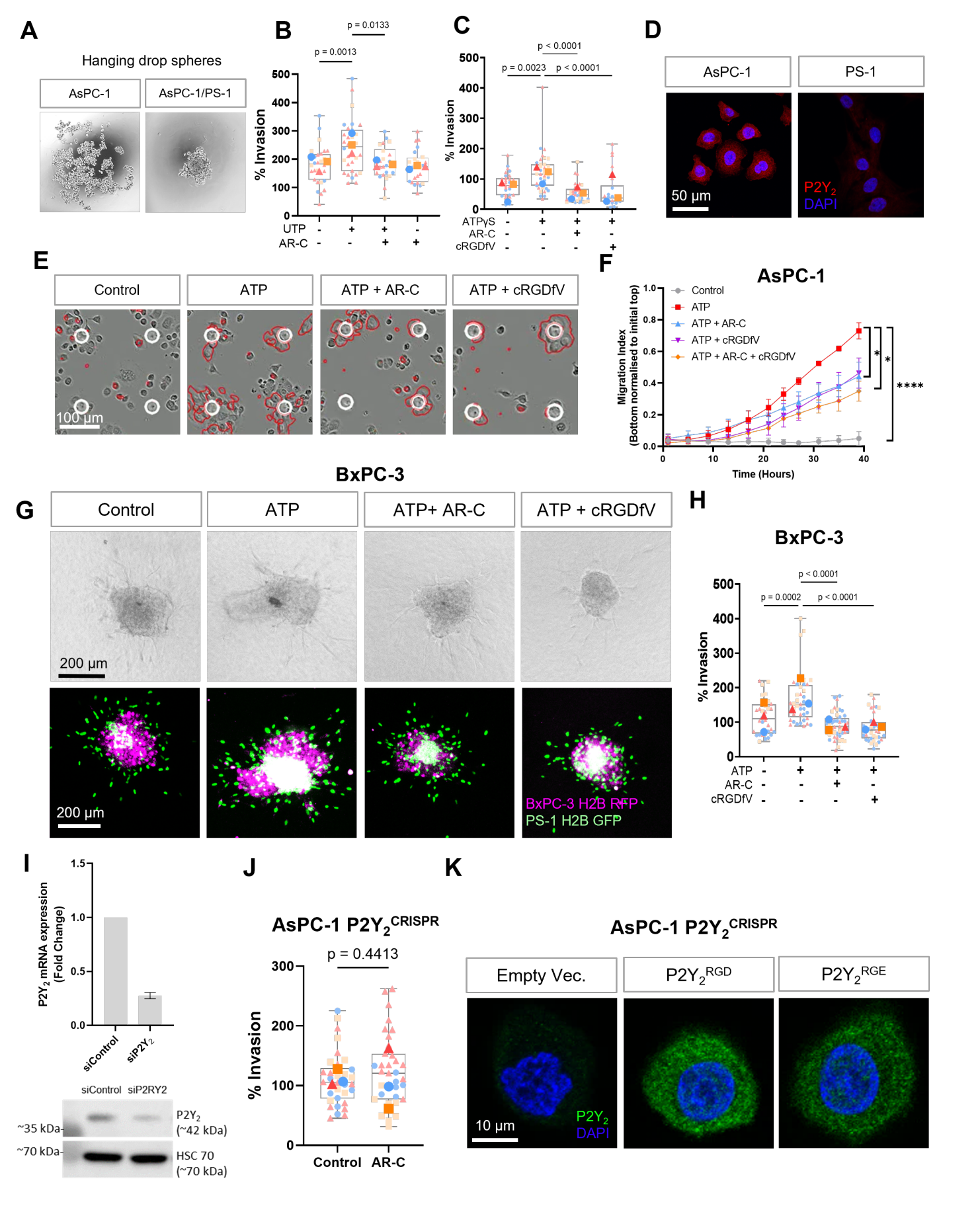
A
Hanging drop spheres
AsPC-1
AsPC-1/PS-1
B
p = 0.0133
p = 0.0013
% Invasion
UTP
AR-C
C
p < 0.0001
p = 0.0023
p < 0.0001
% Invasion
ATPγS
AR-C
cRGDfV
D
AsPC-1
PS-1
50 μm
P2Y2
DAPI
E
Control
ATP
ATP + AR-C
ATP + cRGDfV
100 μm
F
AsPC-1
Migration Index (Bottom normalised to initial top)
Control
ATP
ATP + AR-C
ATP + cRGDfV
ATP + AR-C + cRGDfV
Time (Hours)
BxPC-3
G
Control
ATP
ATP+ AR-C
ATP + cRGDfV
200 μm
200 μm
BxPC-3 H2B RFP
PS-1 H2B GFP
H
BxPC-3
p < 0.0001
p = 0.0002
p < 0.0001
% Invasion
ATP
AR-C
cRGDfV
I
P2Y2 mRNA expression (Fold Change)
siControl
siP2Y2
siControl
siP2RY2
~35 kDa
~70 kDa
P2Y2 (~42 kDa)
HSC 70 (~70 kDa)
J
AsPC-1 P2Y2CRISPR
p = 0.4413
% Invasion
Control
AR-C
K
AsPC-1 P2Y2CRISPR
Empty Vec.
P2Y2RGD
P2Y2RGE
10 μm
P2Y2
DAPI

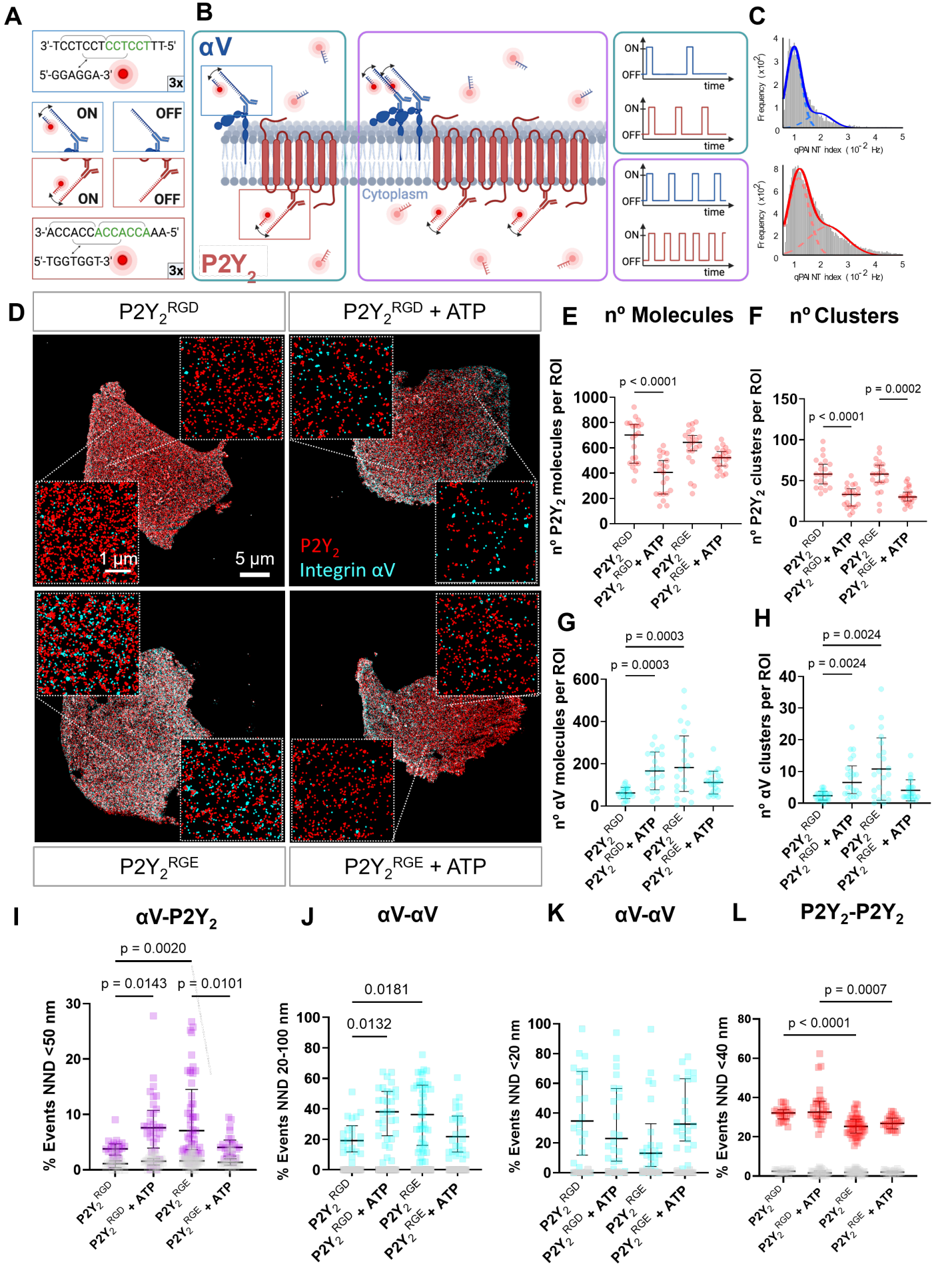
A
3'-TCCTCCTCCTCCTTT-5'
5'-GGAGGA-3'
3x
ON
OFF
ON
OFF
3'-ACCACCACCACCAAA-5'
5'-TGGTGGT-3'
3x
B
αV
P2Y2
Cytoplasm
ON
OFF
time
C
Frequency (x10²)
qPAINT index (10⁻² Hz)
D
P2Y2RGD
P2Y2RGD + ATP
P2Y2RGE
P2Y2RGE + ATP
1 µm
5 µm
P2Y2
Integrin αV
E nº Molecules
nº P2Y2 molecules per ROI
p < 0.0001
F nº Clusters
nº P2Y2 clusters per ROI
p = 0.0002
p < 0.0001
G
nº αV molecules per ROI
p = 0.0003
p = 0.0003
H
nº αV clusters per ROI
p = 0.0024
p = 0.0024
I αV-P2Y2
% Events NND <50 nm
p = 0.0020
p = 0.0143
p = 0.0101
J αV-αV
% Events NND 20-100 nm
0.0181
0.0132
K αV-αV
% Events NND <20 nm
L P2Y2-P2Y2
% Events NND <40 nm
p = 0.0007
p < 0.0001

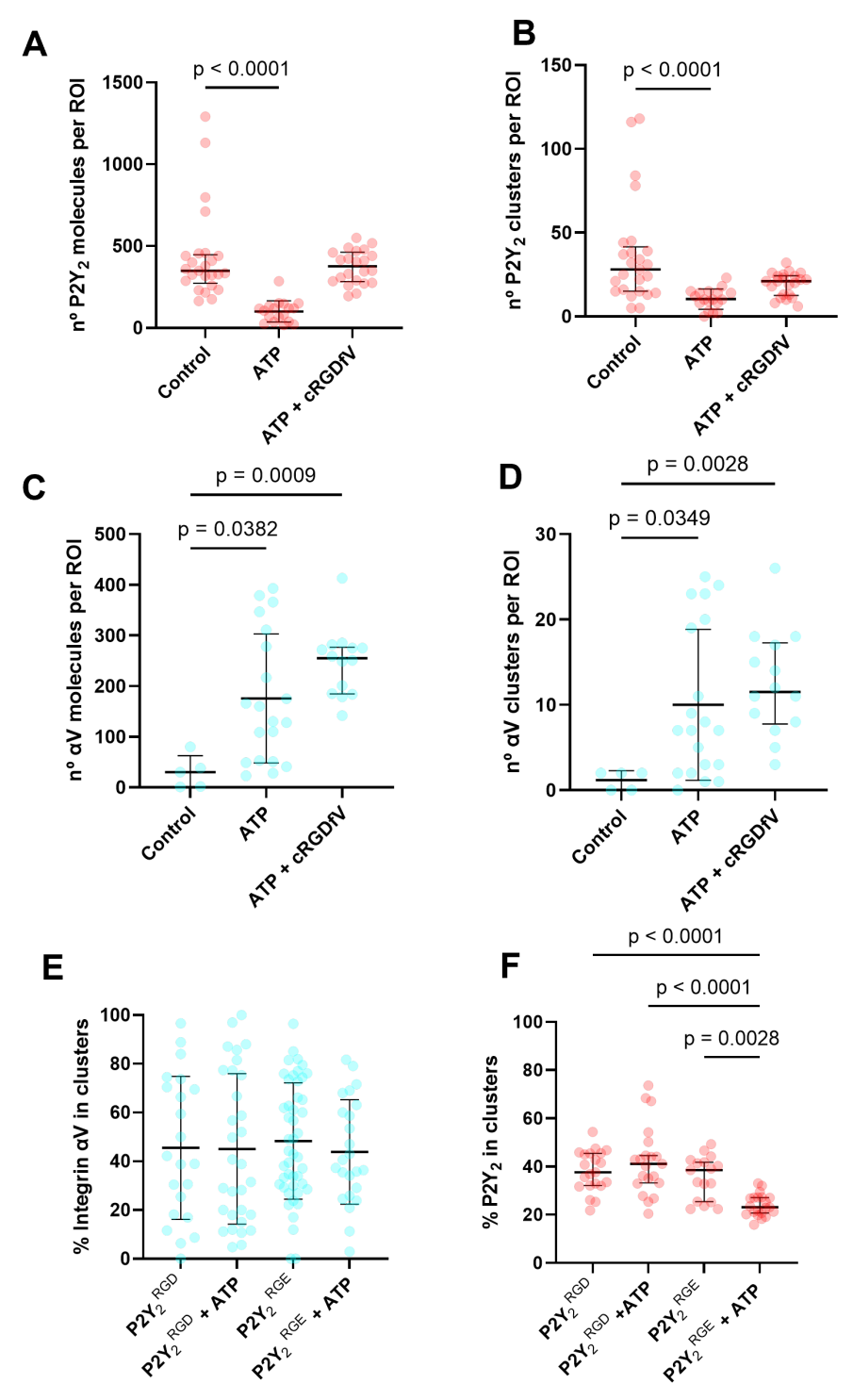
A
p < 0.0001
nº P2Y2 molecules per ROI
1500
1000
500
0
Control
ATP
ATP + cRGDfV
B
p < 0.0001
nº P2Y2 clusters per ROI
150
100
50
0
Control
ATP
ATP + cRGDfV
C
p = 0.0009
p = 0.0382
nº αV molecules per ROI
500
400
300
200
100
0
Control
ATP
ATP + cRGDfV
D
p = 0.0028
p = 0.0349
nº αV clusters per ROI
30
20
10
0
Control
ATP
ATP + cRGDfV
E
% Integrin αV in clusters
100
80
60
40
20
0
P2Y2 RGD
P2Y2 RGD + ATP
P2Y2 RGE
P2Y2 RGE + ATP
F
p < 0.0001
p < 0.0001
p = 0.0028
% P2Y2 in clusters
100
80
60
40
20
0
P2Y2 RGD
P2Y2 RGD +ATP
P2Y2 RGE
P2Y2 RGE + ATP

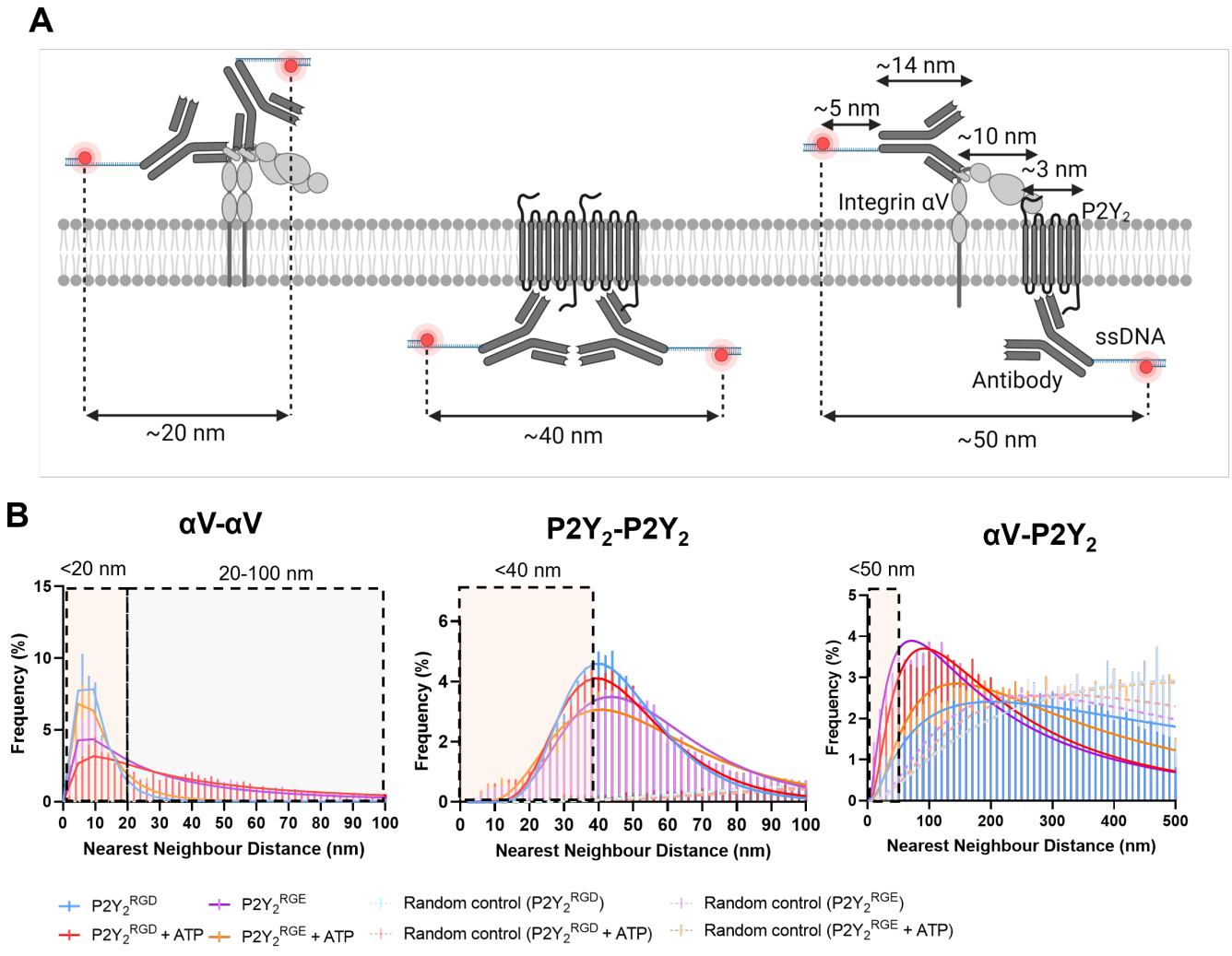
A
~14 nm
~5 nm
~10 nm
~3 nm
Integrin αV
P2Y2
ssDNA
Antibody
~20 nm
~40 nm
~50 nm
B
αV-αV
<20 nm
20-100 nm
P2Y2-P2Y2
<40 nm
αV-P2Y2
<50 nm
Frequency (%)
Nearest Neighbour Distance (nm)
P2Y2RGD
P2Y2RGD + ATP
P2Y2RGE
P2Y2RGE + ATP
Random control (P2Y2RGD)
Random control (P2Y2RGD + ATP)
Random control (P2Y2RGE)
Random control (P2Y2RGE + ATP)

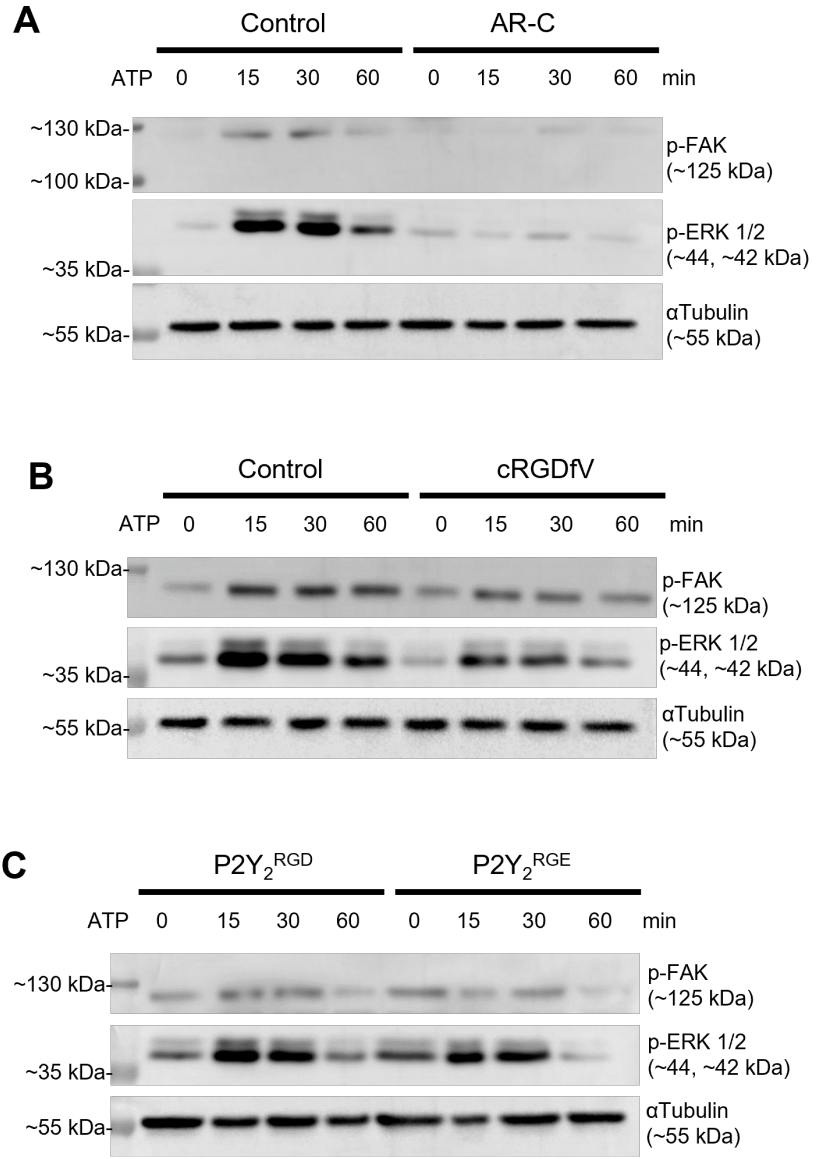
A
Control
AR-C
ATP 0 15 30 60 0 15 30 60 min
~130 kDa-
~100 kDa-
~35 kDa-
~55 kDa-
p-FAK
(~125 kDa)
p-ERK 1/2
(~44, ~42 kDa)
αTubulin
(~55 kDa)
B
Control
cRGDfV
ATP 0 15 30 60 0 15 30 60 min
~130 kDa-
~35 kDa-
~55 kDa-
p-FAK
(~125 kDa)
p-ERK 1/2
(~44, ~42 kDa)
αTubulin
(~55 kDa)
C
P2Y2RGD
P2Y2RGE
ATP 0 15 30 60 0 15 30 60 min
~130 kDa-
~35 kDa-
~55 kDa-
p-FAK
(~125 kDa)
p-ERK 1/2
(~44, ~42 kDa)
αTubulin
(~55 kDa)

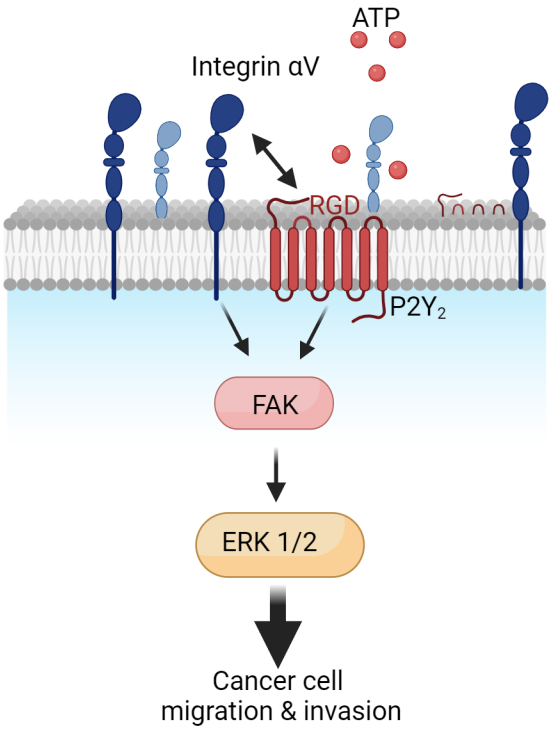
ATP
Integrin αV
RGD
P2Y2
FAK
ERK 1/2
Cancer cell
migration & invasion

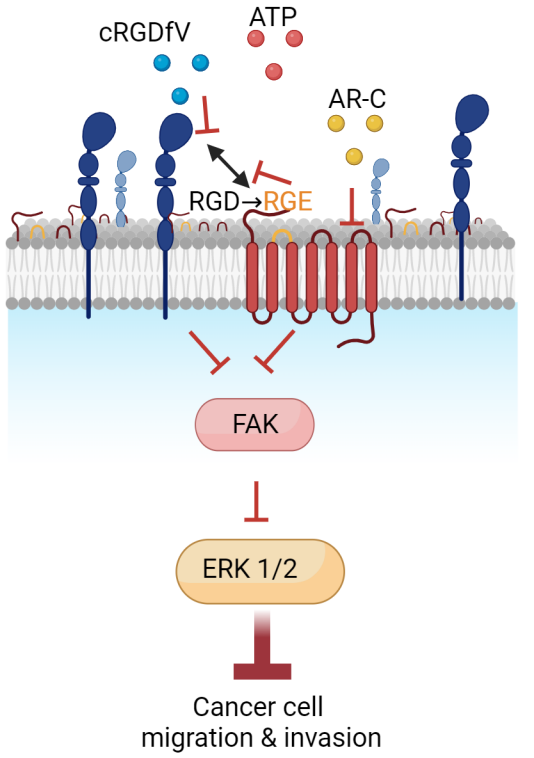
cRGDfV
ATP
AR-C
RGD→RGE
FAK
ERK 1/2
Cancer cell
migration & invasion